POLITECNICO DI TORINO

Master's Degree in Mechanical Engineering

Politecnico di Torino

MASTER's Degree Thesis

Metrological characterization of low stiffness AFM cantilevers for biological applications

Supervisors:

Prof. ALESSANDRO FASANA
Dr. ALESSANDRO SCHIAVI

Candidate:

ISABELLA CAMPOREALE

2024

Contents

Chapter 1

Introduction

1.1 Thesis objective

This thesis work is devoted to providing force traceability at microscale and nanoscale level in the context of Atomic Force Microscopy. Although a procedure exists to ensure metrological traceability to SI units for nanoscale displacements in the X and Y horizontal axes and the Z vertical axis, a method has not yet been developed for ensuring accurate and traceable results for nanoscale forces. To address this, an indirect approach is employed, which derives nano-forces values from the spring constant of the cantilever [1].

For this purpose, Sader's formula [2] was selected and its parameters that contribute to the calculation of the spring constant where investigated along with a detailed uncertainty analysis.

Experimental activities were conducted to measure the resonant frequency and quality factor of several cantilevers, employing the micro Laser Doppler Vibrometer and the Scanning Electron Microscope (SEM) available at INRiM.

Cantilevers of different types and geometries, used in AFM for biological applications, were analyzed, with a thorough assessment of the associated uncertainty budget. To ensure a comprehensive analysis, a type of cantilever intended for mechanical applications was also considered in order to validate the effectiveness of the method in different contexts.

1.2 Atomic force microscopy

Atomic Force Microscopy (AFM) originated as an advancement over Scanning Tunneling Microscopy (STM). Unlike the latter, which is limited to the study of conductive and semiconductive surfaces, AFM offers a wide range of applications due to its ability to analyze nonconductive materials such as polymers, ceramics, composites, glass, and biological samples, among others.
AFM is extensively employed in material science for surface imaging, property measurement, and nanoscale manipulation.
The atomic force microscope (AFM) has established itself as a highly effective instrument for the quantitative measurement of nano-Newton scale forces across various systems but the necessity for precise calibration of AFM cantilevers, the core sensing components of the device, has grown alongside the increasing utilization of AFM for assessing material properties [3].

The interaction forces between the probe tip (mounted on a flexible cantilever) and the sample induce deflections in the cantilever, which reveal the topographical, morphological, or rheological properties of the sample [4].

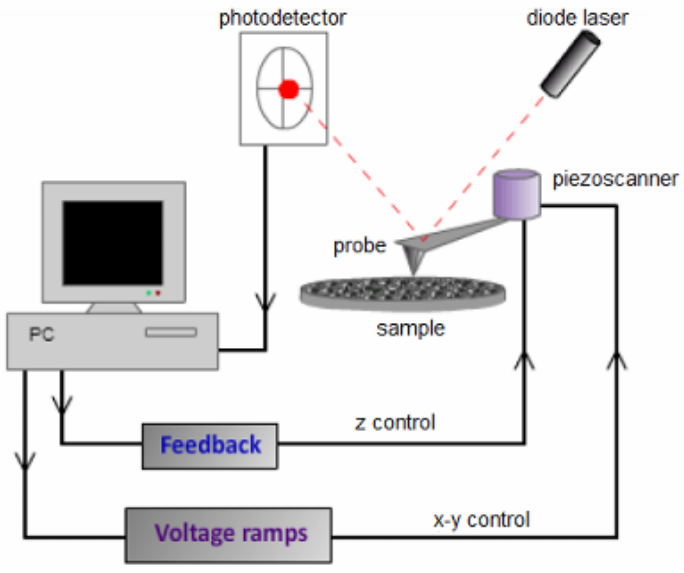

Figure 1.1: AFM main components

The atomic force microscope (Figure 1.1) consists of four basic parts:

- a cantilever equipped with a probe that interacts with the sample,
- a diode laser whose beam is aimed at the back of the cantilever,

- a four-quadrant photodetector that detects the deflection of the cantilever during interaction with the sample surface,

- a piezoelectric scanner that allows the distance between the cantilever and the sample along the z-axis to be adjusted via a feedback mechanism, as well as controlling motion along the x- and y-axes through the application of voltage ramps.

Depending on the interaction forces between the cantilever tip and the analyzed surface, as well as the surface characteristics (material, shape, and surface features), the Atomic Force Microscope (AFM) can operate in three main modes. These modes differ in the relative motion between the cantilever and the surface:

- Contact mode: the sample topography is provided by the deflection of the cantilever which is proportional to the tip-sample interaction forces (see Figure 1.2).

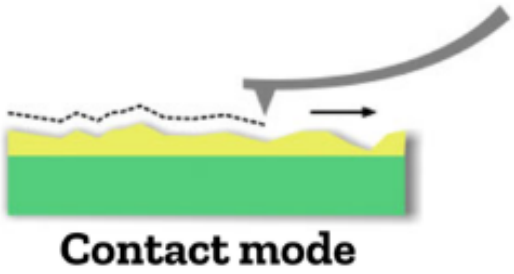

Figure 1.2: Contact mode between cantilever probe and sample surface [5]

- Non contact mode: during measurements the cantilever the cantilever is set into vibration by a piezoelectric actuator, as shown in Figure 1.3, either with constant amplitude and variable frequency or with constant frequency and variable amplitude.

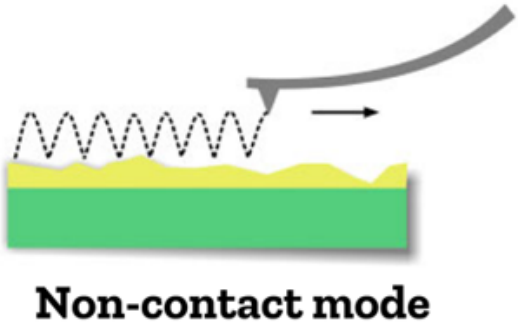

Figure 1.3: Non-contact mode between cantilever probe and sample surface [5]

- Intermitted contact mode or tapping: the cantilever oscillates, so that it contacts the sample cyclically, as illustrated in Figure 1.4, and a force is applied to detach the tip from the sample. As for the non-contact mode, the cantilever is set into vibration by the piezoelectric actuator.

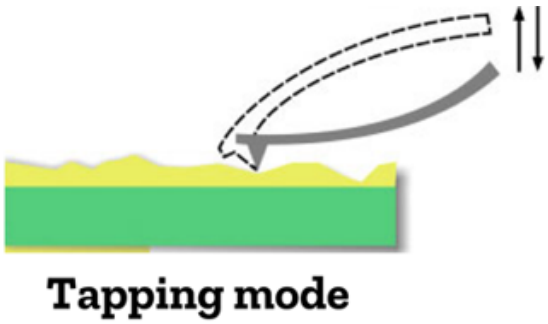

Figure 1.4: Tapping mode between cantilever probe and sample surface [5]

The choice among the AFM's three operating modes depends mainly on the type of sample to be analyzed and the level of reliability required for the results. The contact mode offers higher accuracy, but can damage soft surfaces due to direct contact between the cantilever and the sample, making it more suitable for rigid materials and hard surfaces.

In contrast, the non-contact mode is less invasive because the cantilever does not make direct contact with the sample, but it tends to provide less accurate measurements, especially on soft surfaces.

The tapping mode is frequently used for the analysis of biological samples, as it balances the delicacy of contact with the sample and good resolution, minimizing the risks of damaging the sample during scanning [6].

The interactions between the cantilever probe and the sample in the AFM vary depending on the distance between the two, showing different types of forces at play [7]:

- Long distances: electrostatic forces, due to surface charges, prevail;
- Nanometer distances: Van der Waals forces, related to interactions between molecular dipoles, come into play;
- Direct contact: interactions are mainly elastic, related to the mechanical deformation of the sample.

In the intermediate case between the last two described, it is not easy to determine the force of interaction between probe and sample because of the simultaneous concurrence of attractive and repulsive forces given by molecular probe-sample interactions.

1.3 AFM cantilevers' structure and materials

The typical structure of an AFM cantilever sample consists of a sharp tip placed at the free end of the microcantilever, which is supported at the other end by a tip holder as shown in Figure 1.5. The interaction force between the tip and sample deflects the cantilever.

Given the wide range of applications of AFM cantilevers, there are numerous designs, the most common of which are triangular and rectangular geometries as can be observed in Figure 1.6.

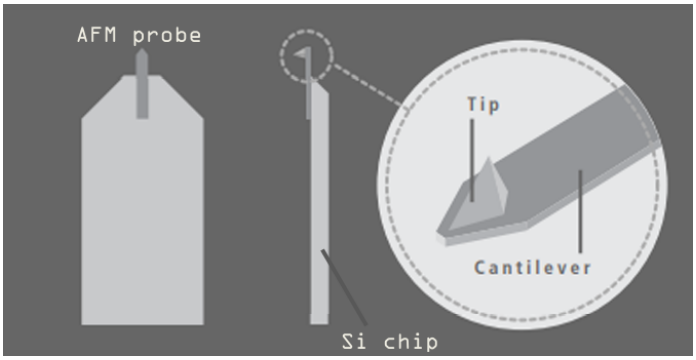

Figure 1.5: Typical structure of an AFM cantilever [8]

The cantilevers are made predominantly of silicon (Si) or silicon nitride (Si_3N_4), while coatings may include gold, especially for biological applications, or platinum or cobalt for other applications. Typical dimensions vary: length ranges between 40 µm and 500 µm, width can be up to 50 µm, and thickness varies between 0.5 µm and 8 µm.

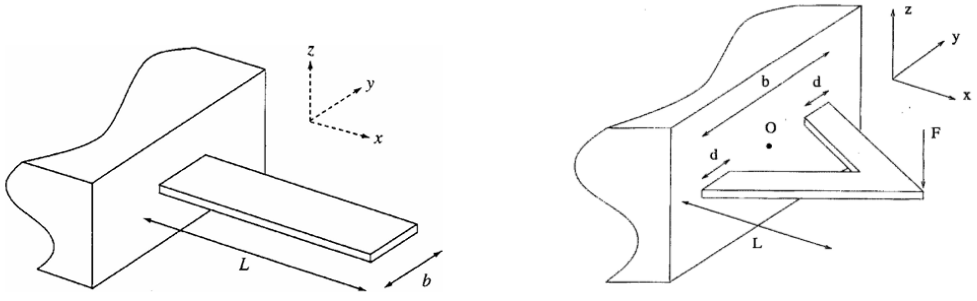

(a) Rectangular cantilever [9] (b) Triangular cantilever [10]

Figure 1.6: Different cantilever geometries

The elastic constant (k) depends largely on the type of application and is typically between 0.01 N/m and 50 N/m [11].

Cantilevers used in AFM can be classified into two main categories based on their elastic constant (k):

- Soft cantilevers: with an elastic constant typically less than 1 N/m, they are mainly used in contact mode and tapping mode. These cantilevers, being less invasive, reduce the risk of damaging delicate surfaces, such as biological surfaces.
- Rigid cantilevers: with an elastic constant generally greater than 1 N/m, they are suitable for non-contact mode applications due to their high resonance frequencies.

This subdivision makes it possible to choose the most suitable cantilever according to the nature of the sample and the mode of operation. Regarding probes, most are pyramidal in shape with a triangular or square base (Figure 1.7) and an opening angle of about 70 degrees, not being overly sharp.

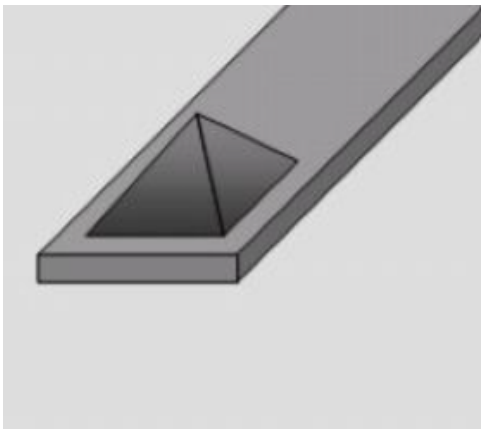

Figure 1.7: Pyramidal probe with square base [12]

However, for investigating samples with steep or deep walls, longer, thinner, and more pointed probes, resembling a stinger (Figure 1.8), are used. These are more suitable for reaching and analyzing intricate features on such surfaces [12].

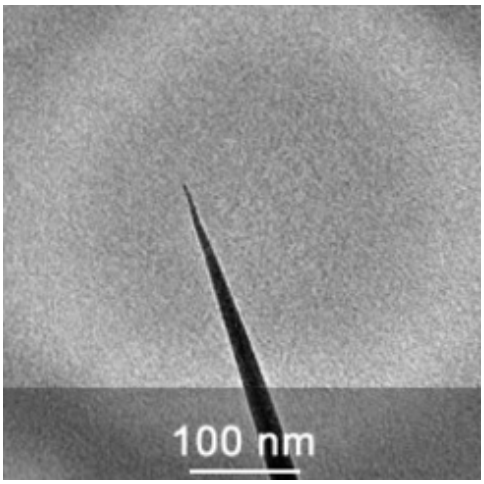

Figure 1.8: Sharper, thinner probe [12]

The spherical probe, shown in Figure 1.9, is less commonly used than the two previously mentioned and is used in applications where the material in contact with the probe is very soft or brittle.

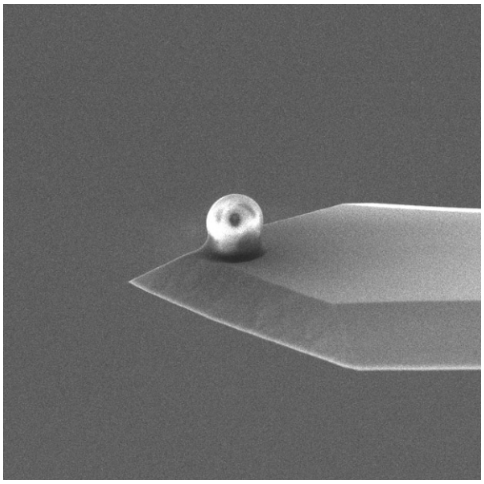

Figure 1.9: Spherical probe [13]

1.4 AFM applications

1.4.1 AFM for Investigating Cell Biophysical Properties

AFM has proven to be an exceptional technique for evaluating cell properties, offering high-resolution images that provide a detailed topological view of the cell. It is a powerful tool for cellular research, enabling nanoscale, non-invasive imaging of cells at an atomic level [14].
This is due to the fact that it works by applying small forces by coming into contact with the surface of the cell, as shown in Figure 1.10, and allows the measurement of the mechanical properties of the cell such as elasticity and stiffness.

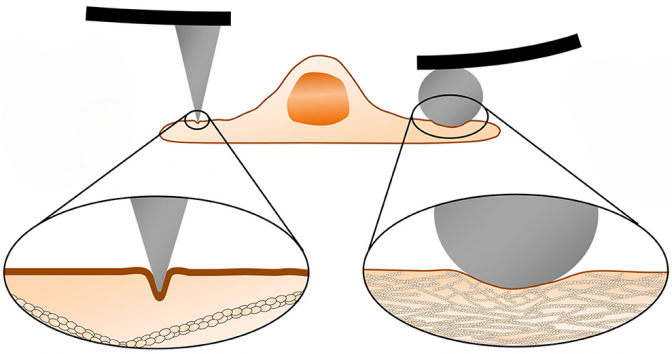

Figure 1.10: Mechanical measurements of cells using AFM [15] with diamond and spherical probes

Through this information, easily measured at different points of the cell thanks to the ease of this method, it is possible to evaluate their variations to identify diseased or potentially harmful cells [16].
AFM has been used, for example, to examine the mechanical properties of both normal and cancerous human bladder cells by measuring their elasticity. This is done by moving a sharp probe across the surface of the cells; when the probe contacts the cell membrane, it applies a small, controlled force and the degree to which the cell deforms under this force is recorded, allowing researchers to determine the stiffness or elasticity of the cell, quantified by Young's modulus. Cancerous and normal bladder cells were examined and the data showed that the cancerous cells were more deformable than normal cells.
More generally, it has been observed that the elastic constant varies between

cancer cells and healthy cells. However, whether this constant is higher or lower in cancer cells than in normal cells depends largely on the type of tumor. Different neoplasms show distinct mechanical properties, with some cancer cells exhibiting greater stiffness, while others are softer than their healthy counterparts [17].

Not only in terms of elastic constant, but other mechanical characteristics of cells, such as surface roughness, have also been observed to vary significantly between malignant and healthy cells.

For example, a significant increase in surface roughness has been documented in leukocytes from leukemia patients compared with healthy white blood cells. Similarly, breast cancer cells showed a rougher surface than normal cells [14]. These findings suggest that AFM measurements could serve as a potential marker for differentiating between normal and cancerous or malignant cells [18].

1.4.2 AFM for investigating mechanical properties of samples

AFM finds wide use in mechanical applications, particularly for the analysis of surface properties. In the case of roughness evaluation, the microscope enables nanometer-accurate reconstruction of sample topography by recording displacement along the axis z, usually operating in contact mode to ensure continuous contact with the surface. In addition, surface analysis by AFM allows other key parameters, such as homogeneity, to be determined and mechanical properties, such as wear resistance, to be obtained indirectly.

1.5 The role of metrological characterization

It is essential that an atomic force microscope is metrologically characterized to ensure the acquisition of accurate and traceable results. Metrological traceability, a cornerstone of modern measurement systems, ensures that instruments produce data that are reliable and comparable to internationally recognized standards. A reportable result, in fact, is intrinsically linked to such standards, enabling comparison and reproducibility of measurements.

In the case of AFM, the relative positions between the cantilever tip and the sample are metrologically characterized and thus referable to the International System (SI). However, in order to metrologically determine the rheological properties of materials, the nanoforces must be referable. Currently, these forces do not possess a recognized referability system.

To fill this gap, we aim to establish the metrological referability of the elastic constant of the cantilever, a crucial quantity to ensure the reliability of nanomechanical measurements.

Accurate characterization of the elastic properties of these cantilevers is essential for the realization of a functional metrological AFM, as it enhances the reliability of quantitative data and experimental findings and is crucial for numerous applications, particularly in the field of mechanical properties of materials. For example, in sensitive imaging, the measurement of forces, that is linked to the elastic constant, becomes essential to ensure that they are not excessively high, as excessively high forces could deform soft materials, compromising the accuracy of the acquired topography and leading to erroneous conclusions regarding the surface structure of the sample [6].

In the biological field, the ability to obtain consistent and repeatable results would be critical in fostering wider use of AFM in clinical and medical applications. In the determination of cellular elasticity, an indicator of many biological properties being studied in the biomedical field, AFM often provides highly variable results.

This variability is mainly due to instrumental errors arising from inaccuracies in the measurement of the elastic constant of the cantilever. Such inaccuracies can compromise data consistency, undermining the reliability of the AFM

as a tool for quantitative biological assessments [16]. In this context, proper metrological calibration of the elastic constant is therefore essential to ensure reliable and reproducible measurements, avoiding errors that could affect the validity of scientific observations.

Knowing the uncertainty associated with measuring the elastic constant of the cantilever also allows to determine a range of variation of the measurement. In this range, if repeated measurements are made, the results will not be able to be adequately distinguished due to instrumental limitations or other uncertainties. In other words, if two measurements fall within the defined range of uncertainty, it is not possible to distinguish with certainty which is the "true" value, since the observed difference may fall within the margins of error established by the instrument used.

Chapter 2

State of the art

2.1 Overview of AFM Measurements

A functional metrological AFM is anticipated to deliver traceable and precise quantification of material properties at the nanoscale. As explored in Section 1.5, metrological AFM facilitates the quantification of both in-plane and out-of-plane topographical, dimensional, and morphological properties of nanoparticles and nanostructures of various types, with sub-nanometer accuracy.

If the applications were not in nano-scale the solution to calculate the deflection would be simply through referred masses, but this becomes difficult in nano-scale because the referability of the masses and their calculation becomes quite complex and imprecise.

To address this shortfall, nanoscale forces are indirectly traced back from the elastic properties of the cantilevers [1]. Determining the elastic constant of a cantilever with accuracy and reportability represents a significant methodological challenge.

Many approaches proposed for its calculation rely on parameters that are difficult to measure accurately, such as the geometric dimensions of the cantilever (length, width and thickness), which are frequently involved in calculation formulas in terms raised to the square or third power.

These parameters, which are essential for calculating the elastic constant, are susceptible to measurement errors that compromise the accuracy of the results. In addition, some methods employ external objects-such as additional masses-to indirectly calculate the elastic constant, but even these objects must

be measured with high precision, introducing additional uncertainties.
These inherent difficulties greatly complicate obtaining a reliable and repeatable value of the elastic constant, which is essential to ensure correct measurements in metrology applications conducted by AFM.

2.2 Existing methods for the characterization of cantilever beams

Numerous theoretical and experimental methods have been developed to calibrate AFM cantilevers, with a primary focus on determining the spring constant. Although the term "calibration" is widely used within the AFM community, it is not entirely appropriate when referring to the evaluation of these elastic properties. A more accurate term would be "metrological characterization." Nevertheless, to maintain consistency with common practice, we will continue to use "calibration" as a synonim in this context.
The methodologies that have been explored in recent years can be categorized into three main categories which will be explored in more detail in the next sections.
It should be remembered, however, that the purpose of this thesis is not to compare these methodologies, but rather to show the motivations that led to the choice of Sader's method rather than others and this will be explained considering the limitations of each method.

2.2.1 Dimensional method

The first methodology for calibrating AFM cantilevers is known as the dimensional method. This approach is based on the precise measurement of the cantilever's geometrical properties, such as its length, width, and thickness, using advanced dimensional techniques.
By accurately determining these physical dimensions, it is possible to estimate the cantilever's spring constant, which plays a crucial role in its mechanical response.
This method offers a straightforward and non-invasive means of calibration, relying solely on the physical characteristics of the cantilever, without requiring complex external forces or interactions.
Among the methods that rely most heavily on the dimensional characteristics of the cantilever to determine the elastic constant, one of the best known is the Euler beam equation (2.1) which is based on the assumption that the

cantilever acts as an elastic beam subjected to an applied force:

$$k = \frac{Et^3w}{4L^3} \tag{2.1}$$

where:

- E is the elastic modulus,
- t is the thickness of the cantilever,
- w is the cantilever's width,
- L is the lenght of the cantilever.

Or in the case where the cross section of the cantilever is not rectangular, the equation becomes:

$$k = \frac{3EI}{L^3} \tag{2.2}$$

where I the moment of inertia of the cantilever beam.
However, this method is accurate mainly for rigid cantilevers and does not provide reliable results in the case of soft or very soft cantilevers, particularly those with an elastic constant less than 0.1 N/m, where the deformations are no longer well described by Euler's approach [19].

2.2.2 Static experimental methods

Static experimental method for calibrating the spring constant and effective mass of AFM cantilevers rely on direct measurement of external reference properties such as known masses.

In particular, a well-known static method involves attaching known masses to the cantilever tip and measuring the resulting changes in resonant frequency. AFM cantilevers, typically V-shaped or rectangular in cross-section, can be modeled as simple rectangular beams, with V-shaped cantilevers approximated by two parallel rectangular beams [20]. This allows the system's dynamics to be described using relatively simple theoretical models.

However, while theoretically sound, this method may present limitations in practice. It relies on several approximations, particularly in modeling cantilever geometry, and is sensitive to experimental inaccuracies in mass addition and frequency measurement. Furthermore, attaching masses can alter the cantilever's mechanical properties, introducing non-ideal effects that compromise the precision of the spring constant determination.

Another significant limitation of this method is that, as in the case of nano forces, the additional masses used do not possess nanometer-level traceability, and therefore its accuracy is highly dependent on the precision with which these masses are measured.

Since the method relies on this measurement to determine the elastic constant of the cantilever, any uncertainty in the quantification of the masses introduces a significant margin of error into the results.

Another static method used to determine the elastic constant of the cantilever, which originated as a variation of the additional masses method, is to use a focused ion beam (FIB) to remove a defined volume from the cantilever, thus reducing the uncertainty introduced by the external masses [21]. Although this approach can improve accuracy, it has limited applications. In fact, the results are repeatable and reportable only if the cantilever is made of silicon and possesses an elastic constant greater than 0.7 N/m.

This limitation makes the method of little use for metrological characterization of very soft cantilevers, such as those used in biological applications, where the

elastic constant is often less than this value.

In general, considering both the mass method and the method based on the use of focused ion beam (FIB), both have significant limitations in terms of accuracy and variety of application.

These methods are not ideal for comprehensive metrological characterization across all types of cantilevers, as they can be difficult to implement, require complex set-up, or are invasive, especially for soft cantilevers.

2.2.3 Dynamic methods

Dynamic methods for calibrating the spring constant of AFM cantilevers are grounded in analyzing the cantilever's resonant response [6].
Unlike static methods, which often involve physical interaction with the cantilever, dynamic techniques offer a non-invasive approach by exploiting the cantilever's vibrational characteristics. This approach is particularly beneficial for accurately determining cantilever properties without introducing external forces or altering the cantilever's natural behavior.

Among the dynamic methods, three key methods stand out for their effectiveness and widespread use: the Cleveland method, the thermal noise method and the Sader method.
The Cleveland method utilizes changes in resonant frequency to infer the spring constant, offering a straightforward yet robust calibration approach [20].
Through this method the elastic constant is calculated with the formula:

$$k = 2\pi^3 w L^3 \left(\frac{\rho_{lever}^3}{E} \right)^{1/2} f_R^3 \tag{2.3}$$

where:

- ρ_{lever} is the density of the cantilever;
- f_R is the resonant frequency;
- $w,\ L$ are the dimensional parameters;
- E is the Young Modulus of the cantilever.

The cantilever's density and Young's modulus are often nominal values, which inevitably introduces uncertainties. In the thermal noise method, the average energy of the cantilever is related to its thermal oscillation, this approach therefore uses thermal fluctuations to determine the elastic constant without applying external forces [22]:

$$k = \frac{k_B\ T}{\chi^2} \tag{2.4}$$

where:

- k_B is the Boltzmann constant,
- T is the temperature in Kelvin,
- χ is the thermal noise which is the area subtended by the resonance frequency peak.

Sader's method determines the elastic constant of the cantilever by considering a combination of dimensional parameters, dynamic parameters of the cantilever and hydrodynamic parameters of the surrounding fluid. The formula used will be analyzed in more detail in Section 3.1.1.
These dynamic methods provide significant advantages in terms of accuracy and non-invasiveness.

2.2.4 Advantages in employing Sader's method

Sader's method is widely used for the metrological characterization of cantilevers because of its accuracy and repeatability.
It is also distinguished by the fact that it does not require the use of external elements such as additional masses and is noninvasive.
The uncertainties associated with this method are generally lower than those of the thermal noise method [23], and, by introducing an invariant term, the formula does not depend on either the mass or the density of the cantilever, as in Cleveland's method, which are parameters difficult to determine with metrological accuracy and traceability.
Sader's method is also used for the calibration of cantilevers in the biological field, including applications involving cantilevers immersed in different types of hydrogels [16], in order to minimize errors associated with the calculation of the elastic constant.
From the standpoint of determining the uncertainty budget, Sader's formulation also allows easy identification of the parameters that contribute most to the final uncertainty of the cantilever, allowing these parameters to be refined once identified. In particular, the determination of the quality factor that appears in Sader's formulation seems to be one of the most influential parameters, along with dimensional measures, in increasing the overall uncertainty.
Therefore, in this thesis, significant effort was also devoted to improving the uncertainty related to these parameters, also with the help of use advanced tools such as the Micro Laser Doppler Vibrometer and the Scanning Electron Microscope (SEM) available at INRiM.

Chapter 3

Metrological characterization of Cantilevers

3.1 Description of the method

3.1.1 Sader's method

The Sader equation that will be used for this thesis, starts from the governing equation for the dynamic deflection of a thin plate that has small deflections [9]. Compared to the classic mass-spring system, a thin plate is a continuous body, therefore the mass is not concentrated in a single point but is distributed along its entire surface and for this reason, density rather than mass appears in the formula.

$$D\nabla^4 w(x,y,t) + \sigma\frac{\partial^2 w(x,y,t)}{\partial t^2} = q(x,t,t) \tag{3.1}$$

where σ is the mass per unit area of the plate, q is the external transverse loading per unit area and D represents the flexural rigidity:

$$D = \frac{Eh^3}{[12(1-\nu^2)]} \tag{3.2}$$

where E is Young's modulus, ν is Poisson's ratio, and h is the thickness of the plate. The deflection and the external transverse load are in function of the spatial coordinates x and y and of time t. This (PDE) is nothing more than a more specific version of the Euler-Bernoulli equation. Sader solves eq 3.2 under appropriate boundary conditions, mentioned in [24], and with the aim of finding first the resonance frequency, not the deflection function. To do this Sader decides to use the effective mass M_e, a quantity that is invariant under

certain conditions which is the fraction of two quantities, λ_k and λ_ω. This concept derives from the Rayleigh method [25], which is often used in mechanical engineering; it reasons on the concept of total energy s conservation, composed of kinetic energy and potential energy. Rayleigh therefore state that the ratio between these two quantities must remain unchanged, consequently obtaining the so-called Rayleigh quotient. With a similar reasoning Sader then introduced the terms λ_k and λ_ω:

$$\lambda_k = \frac{\alpha^2 k}{D} \tag{3.3}$$

$$\lambda_\omega = \omega \alpha^2 \sqrt{\frac{\sigma}{D}} \tag{3.4}$$

where α is the root square of the area of the plate, k is the elastic constant, while the other quantities have already been described in the section above. The ratio between these two quantities gives:

$$M_e = \frac{\lambda_k}{\lambda_\omega} = \frac{k}{m\omega^2} \tag{3.5}$$

Finally, Sader, studied the dependence between M_e and the ratio L/b of the cantilever, length and width respectively, and deduced that the effective mass remains an almost invariable quantity for ratios of L/b as shown in Figure 3.1 that exceed approximately 4, and it is:

$$M_e = 0,2427 \tag{3.6}$$

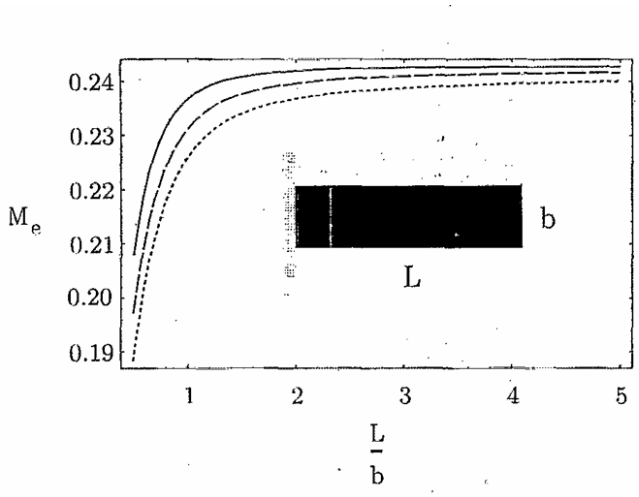

Figure 3.1: Effective mass in function of L/b ratio [9]

and which is also an dimensionless quantity. Without delving into the theoretical background of the analytical demonstration, the formula obtained after numerous mathematical steps for the determination of the elastic constant is:

$$k = M_e \rho_c b h L \omega_{vac}^2 \tag{3.7}$$

where ω_{vac} is the fundamental resonant frequency of the cantilever in vacuum, L, b and h are the length, width and thickness of the cantilever respectively, ρ_c is its density and M_e is the previously introduced effective mass term. Considering that the resonant frequency in vacuum can be written in relation to the resonant frequency in fluid ω_f introducing the hydrodynamic function Γ, specifically its real part, and the density of the fluid ρ_f as:

$$\omega_{vac} = \omega_f \left(1 + \frac{\pi \rho_f b}{4 \rho_c h} \Gamma_r(\omega_f)\right)^{1/2} \tag{3.8}$$

and considering that the term $\rho_c h$ can be substituted by:

$$\rho_c h = \frac{\pi \rho_f b}{4} \left[Q_f \Gamma_i(\omega_f) - \Gamma_r(\omega_f)\right] \tag{3.9}$$

where Γ_i is the imaginary part of the same hydrodynamic function and Q_f is the quality factor in fluid. Combining these equations and using the resonant frequency in Hertz f_R instead of the angular resonant frequency in the formula we obtain that the dynamic spring constant:

$$k = 7,5246 \rho_{air} b^2 L \Gamma_i(Re) f_R^2 \tag{3.10}$$

which is our final equation.

3.1.2 Effective value of the dynamic spring constant

In many cases, the cantilever probe, which coincides with the position in which the load is applied, is positioned not exactly at the tip of the cantilever but 10-15% back from it [9], a distance that is referred to as ΔL. For this reason, the calculated spring constant, which assumes that the load is placed at the tip of the cantilever, turns out to be lower than expected. To obtain the effective

value of the spring constant of the cantilever, the following formula is used:

$$k_{eff} = k \left\{ \frac{L}{L - \Delta L} \right\} \tag{3.11}$$

3.1.3 Rasmussen's model

To calculate the properties of the air that are included both directly in the final formula and in the calculation of the Reynolds number from which the hydrodynamic function is derived, the Rasmussen method was used, which is the method that is currently being employed for the calibration of microphones on an international standard [26]. According to Rasmussen's model we can calculate the air density from:

$$\rho_{air} = 3,84349 \cdot 10^{-3} \frac{p_s}{ZT}(1 - 0,378 \cdot x_w) \tag{3.12}$$

and the air dynamic viscosity from:

$$\mu_{air} = (a_0 + a_1 T + (a_2 + a_3 T)x_w + a_4 T^2 + a_5 x_w^2) \cdot 10^{-8} \tag{3.13}$$

where the a_n terms are given in [26], x_w is the molar fraction of water vapor in air as a function of experimental relative humidity RH, static pressure p_s, enhancement factor $f(p_s, T)$, and saturation water vapor pressure $p_{sv}(T)$ In this reference [26] , the formula for calculating the compressibility factor $Z(p_s, T, x_w)$, along with the definition of the associated terms, is also provided.

3.1.4 Hydrodynamic function

As mentioned in the previous Section, the Reynolds number is used as an intermediate result to be able to calculate the imaginary part of the hydrodynamic function that appears in the final Sader's formula. For a beam with circular cross section the formula for the hydrodynamic function $\Gamma_{circ}(\omega)$ is [27]:

$$\Gamma_{circ}(\omega) = 1 + \frac{4iK_1(-i\sqrt{iRe})}{\sqrt{iRe}K_0(-i\sqrt{iRe})} \tag{3.14}$$

where K_0 and K_1 are the modified Bessel function of the third kind, in which the variable is $-i\sqrt{iRe}$, where Re is the Reynold's number, calculated as:

$$Re = \frac{\rho_{air}\omega_0 b^2}{4\mu_{air}} \tag{3.15}$$

where ρ_{air} and μ_{air} have been calculated through Rasmussen's model. To calculate the hydrodynamic function for rectangular cantilevers, which is the one needed for our case of study, a correction $\Omega(\omega)$ is applied to the hydrodynamic function of circular beams $\Gamma_{circ}(\omega)$. The hydrodynamic function for the rectangular beam $\Gamma_{rect}(\omega)$ can then be expressed as:

$$\Gamma_{rect}(\omega) = \Omega(\omega)\ \Gamma_{circ}(\omega) \tag{3.16}$$

This correction $\Omega(\omega)$ is a complex number were both the real and the imaginary part are a rational function of $\tau = log_{10}Re$.

$$\Omega_r(\omega) = \sum_{n=0}^{6} \left(A_n \tau^n\right) \left(B_n \tau^n\right)^{-1}, \tag{3.17}$$

$$i\Omega_i(\omega) = i \sum_{n=0}^{6} \left(C_n \tau^n\right) \left(D_n \tau^n\right)^{-1}. \tag{3.18}$$

Where the numerical coefficients of the fit regression A_n, B_n, C_n, D_n are provided in explicit form in [27]. In Figure 3.2 the relationship of the various terms and how they contribute to the final formula are depicted.

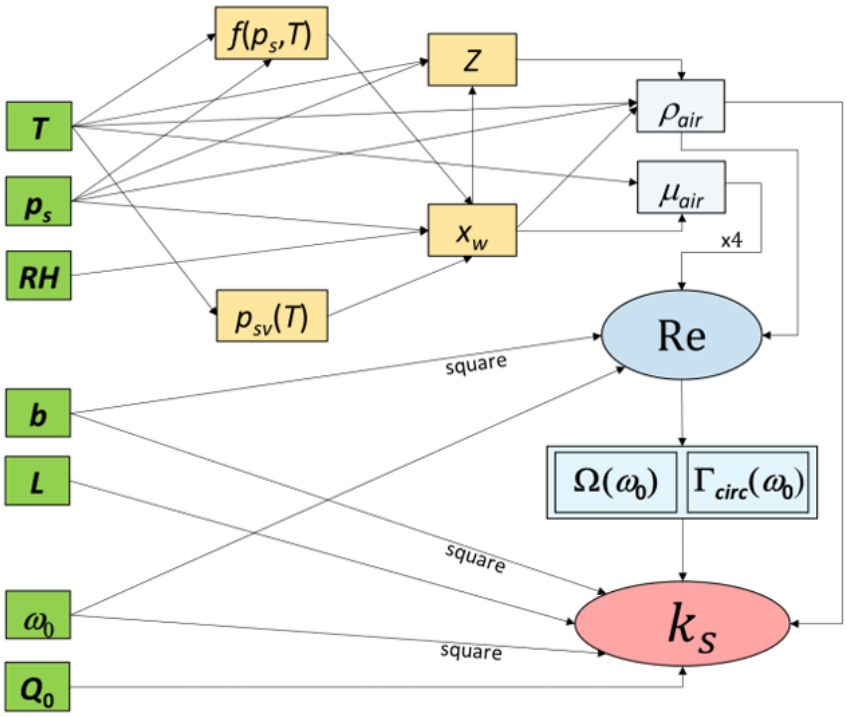

Figure 3.2: Flowchart of Sader's parameters' relationships

3.2 Determination of uncertainties

An in-depth analysis of uncertainty budget is expected to provide useful information with the aim to improve the measurement precision of AFM cantilever spring constant, supporting the "provisional" force traceability at nanoscale. For definitions of guidelines for evaluating measurement uncertainties in metrology, reference is made to the Guide to the Expression of Uncertainty in Measurement, also called GUM. It represents an international reference standard to ensure uniformity in the definition of uncertainties in scientific results.
Each constituent parameter of Sader's formula x_i is associated with its uncertainty $u^2(x_i)$. The calculation of the standard uncertainties, $u^2(x_i)$, depends on their classification type [28]:

- type A uncertainties, that are associated with input quantities that randomly vary, are calculated as the square of the experimental standard deviation or as the square of half-width of the interval of variability.

- type B uncertainties, that are related to input quantities that have not been obtained from repeated observations, are evaluated by scientific judgment based on all the available information on the variability of the input quantity.

Considering the parameters included in Sader's formula and therefore the parameters that are used to obtain them in particular can be classified in the following way:

- dimensional quantities such as b, L, ΔL and dynamic quantities such as f_R and Q, have related standard uncertainties of type A because of their intrinsic variability;

- quantities related to the air properties, i.e. the surrounding fluid in which the cantilever is immersed, are determined by propagating type B uncertainties so air temperature (T), relative humidity (RH), and static atmospheric pressure (p_s), are provided according the instruments proper resolution.

Finally, the extended uncertainty of the spring constant is derived, considering the combination of the standard uncertainties of the input estimates. The GUM states [28]:*"The standard uncertainty of y, where y is the estimate of the measurand Y and thus the result of the measurement, is obtained by appropriately combining the standard uncertainties of the input estimates* $x_1, x_2, ..., x_N$*. This combined standard uncertainty of the estimate y is denoted by* $u_c(y)$*". The combined standard uncertainty* $u_c(y)$ *is the positive square root of the combined variance* $u_c^2(y)$*, which is given by:*

$$u_c^2(y) = \sum_{i=1}^{N} \left(\frac{\partial f}{\partial x_i} \right)^2 u^2(x_i) \tag{3.19}$$

The expanded uncertainty $U(y)$ is then obtained by multiplying the combined standard uncertainty $u_c(y)$ by a coverage factor k_p which depends on a preferred level of confidence in percentage. For this study, a confidence level of 95 % was chosen and consequently a coverage factor of $k = 2$.

3.3 Description of the measurand

Measurements were made on six different types of cantilevers and, where possible, at different points along the length of the cantilever itself.

MikroMasch CSC38

The HQ Series AFM probes are designed for use in soft-contact applications, with three distinct cantilevers integrated onto a single carrier chip. These probes are designed for versatility in a variety of scanning scenarios.

Key attributes of the HQ Series include a consistent AFM tip radius, optimized cantilever reflectivity, and reliable quality factor. The probes are coated with a 30 nm layer of gold over a 20 nm underlayer of chromium, providing both electrical conductivity and chemical inertness. This coating improves laser reflectivity for improved performance in both air and liquid environments. The coated tips maintain a radius of less than 35 nm, ensuring accuracy during measurements.

The coating process may induce a slight flexure in the cantilever, with flexures of up to 3°. However, this effect is controlled and does not significantly impact their performance in typical applications.

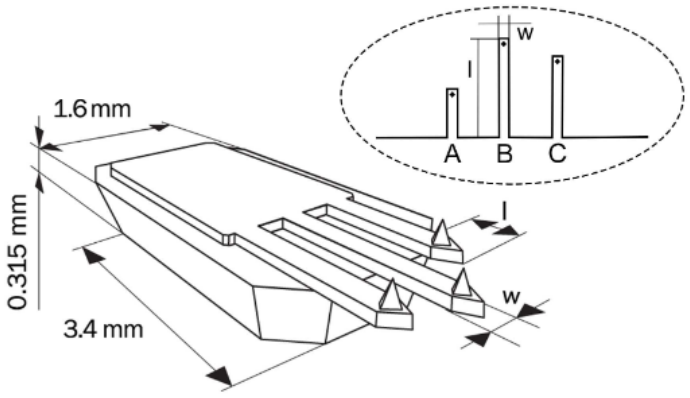

Figure 3.3: Schematic of CSC38 cantilever
(all dimensions are nominal)

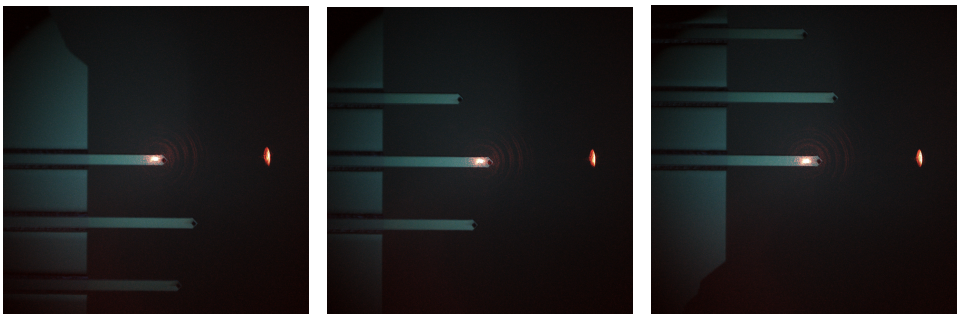

(a) Cantilever A (b) Cantilever B (c) Cantilever C

Figure 3.4: CSC38 seen from the microscope lens

MikroMasch XSC11

The HQXSC11 series AFM probes feature four different cantilevers, two on each side of the carrier chip, and are designed for a wide range of applications.

These probes provide high uniformity of AFM tip beam, cantilever reflectivity, and quality factor.

The cantilevers feature a wear-resistant 20 nm diamond-like carbon (DLC) coating on the tip side. This coating is chemically inert and more hydrophobic than silicon with a natural oxide layer. On the reflective side, an aluminum coating increases the laser reflectivity of the cantilevers by approximately 2.5 times, improving their efficiency.

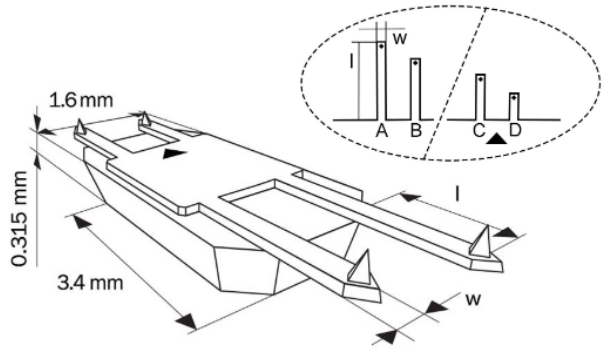

Figure 3.5: Schematic of XSC11 cantilever
(all dimensions are nominal)

This cantilever was found to be particularly fragile, as all those of this type showed at least two broken tips out of four, it was decided to analyze the intact side of one of the cantilevers supplied, respectively tip A and tip B.

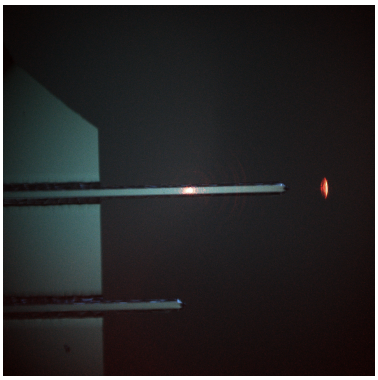

Figure 3.6: XSC11 tip A and B seen from the microscope lens

Bruker NPG10

The Bruker NPG10 cantilever is made of silicon nitride, with a triangular geometry and 4 cantilevers. Its structure has a nominal thickness of 0.6 µm, with a variable thickness between 0.4 and 0.7 µm. The back surface is coated with a reflective gold, while the top side is made of a Ti/Au layer with a thickness ranging from 45 to 5 nm. This type of cantilever is designed for low bending, with a bend specification of no more than 2 degrees. Precise cantilever orientation is important to avoid excessive stress, and DNP is recommended for bending less than 4 degrees, especially for Bruker Dimension SPMs.

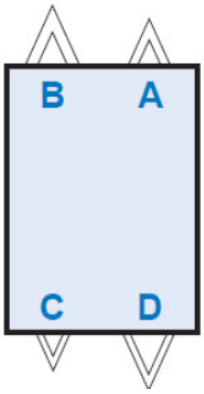

Figure 3.7: Schematic of XSC11 cantilever

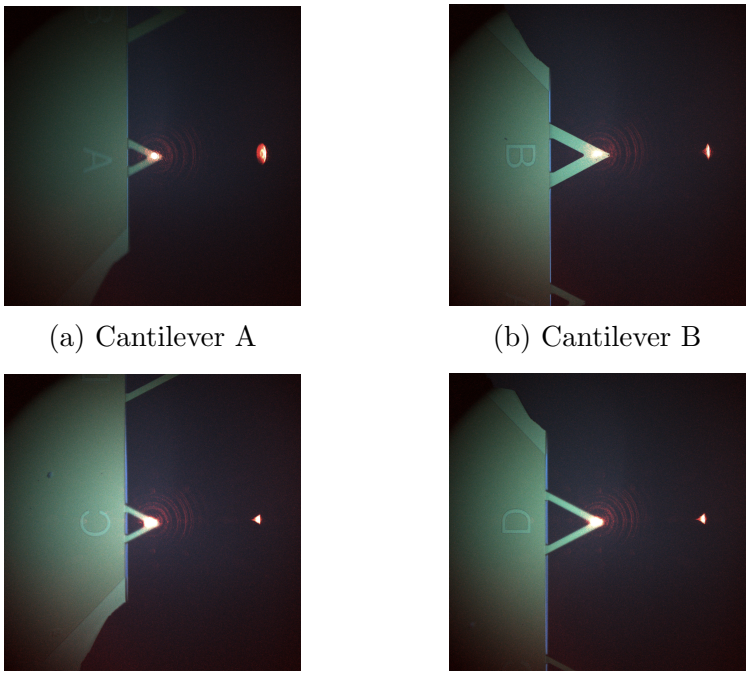

(a) Cantilever A (b) Cantilever B

(c) Cantilever C (d) Cantilever D

Figure 3.8: CSC38 seen from the microscope lens

Nanosensors Atec ContAu-10

Nanosensor Atec ContAu cantilevers are particularly suitable for samples with small pattern sizes and steep sample features, due to their small half-cone angles. The AFM tip has a height ranging from 15 to 20 µm and has a high mechanical Q-factor, which ensures higher sensitivity during measurements. The gold coating consists of a double layer of chromium and gold, approximately 70 nm thick, applied to both sides of the cantilever. The coating on the tip gives the cantilever better conductivity, allowing electrical contacts, while the coating on the detector side increases the reflectivity of the laser beam by approximately two times, while preventing light interference inside the cantilever. The coating process is optimized to reduce stress and increase wear resistance, resulting in the cantilever bending due to stress being less than 2 degrees. The schematic in this case is not provided as it consists of a single tip on the tip holder.

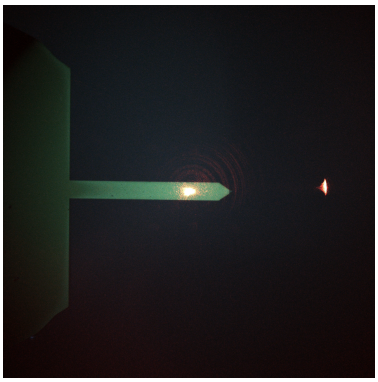

Figure 3.9: Atec ContAu-10 seen from the microscope lens

Olympus Biolever

The BioLever is a cantilever designed for advanced AFM applications, ideal for studying biomolecules and biological samples in liquid environments. With its short length of about 40 micrometers, it offers greater sensitivity and a rapid response to changes in the shape of biomolecules, reducing relaxation times. Its geometry minimizes thermal noise and damping in water, allowing for fast and precise scanning.

The double-layer silicon tip makes it ideal for detailed observations of DNA, proteins and cells. In addition, the silicon nitride cantilever reduces autofluorescence, making it compatible with AFM systems combined with fluorescence microscopes.

Designed specifically for use in liquid, the BioLever mini offers high resonance, allowing for fast and precise acquisition even on complex samples, and includes pre-separated chips for immediate and convenient installation. The Biolever has very small dimensions compared to other cantilevers and this allows it to have a very high resonant frequency despite having the lowest Young's modulus. The schematic in this case is not provided as it consists of a single tip on the tip holder.

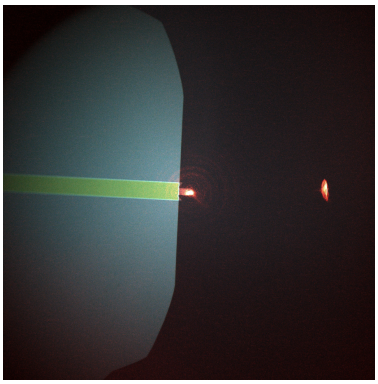

Figure 3.10: Biolever seen from the microscope lens

ParkSystems PPP NCHR

The PPP-NCHR model, produced by Nanosensors, is a cantilever characterized by a high resonance frequency. This is the only sample among the studied cantilevers to have a high stiffness and to be used mainly for mechanical applications, such as evaluating the roughness of the surface; it was therefore decided to include thisdifferent type of cantilever among those used mainly for biological applications to evaluate the validity of the method also in different contexts. The tip has a typical length between 10 and 15 μm and a radius less than 10 nm, making it suitable for high-precision measurements. With a spring constant of about 42 N/m and a resonance frequency of about 330 kHz. The schematic in this case is not provided as it consists of a single tip on the tip holder.

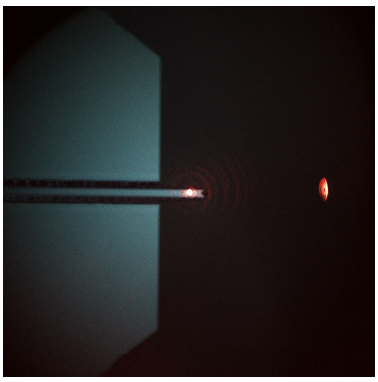

Figure 3.11: PPP-NCHR seen from the microscope lens

3.4 Description of the measurement system

The dynamic vibrational response, encompassing resonance and damping characteristics, was evaluated using the micro-Laser Doppler Velocimetry (μ-LDV) technique. These quantities are determined by measuring the resonance frequency ω_0 and the quality factor of the cantilever Q_0, by using a μ-LDV, namely a Polytec laser Doppler vibrometer based on VibroFlex Connect front and VibroFlex Compact sensor, with integrated camera and VIB-A-20XLENS microscope lens.

The power of the laser is 1 mV and the laser spot size is about 2 µm^2.

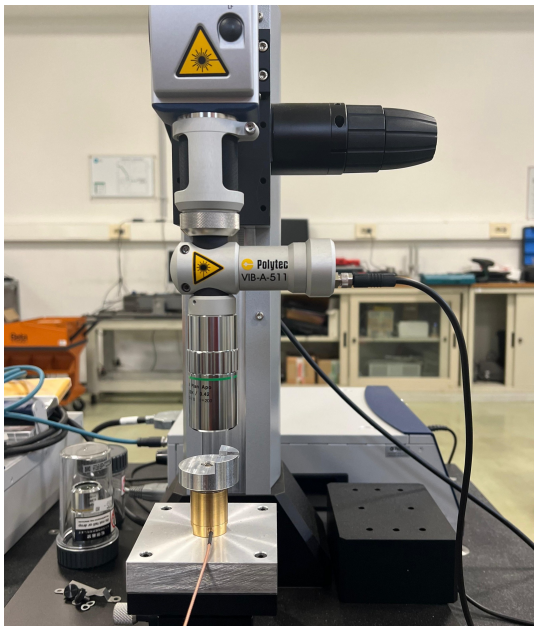

Figure 3.12: μ-LDV (Polytec laser Doppler vibrometer)

The cantilever is fixed on a proper support opportunely designed and realized, shown in Figure 3.13, the μ-LDV is placed on an active anti-vibration table.

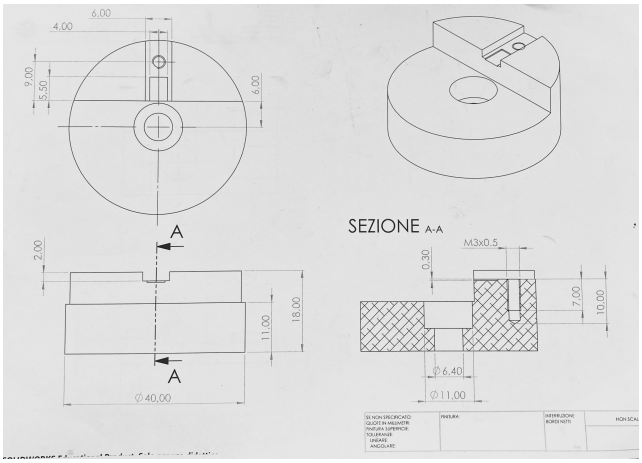

Figure 3.13: Design of the support

The frequency analysis is carried out by using a NI PXIe-1071, with a sensitivity of $2,5 \cdot 10^3$ m/s^2/V, and a bandwidth of 500 kHz.

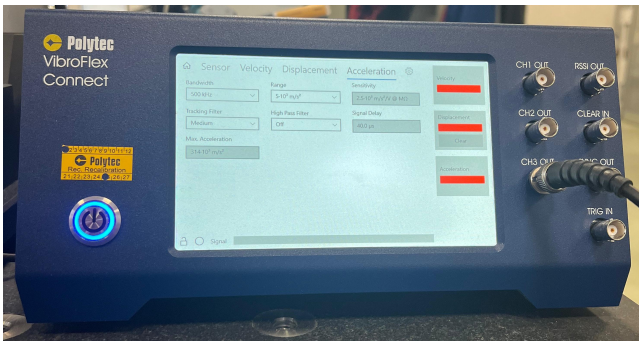

Figure 3.14: Settings for signal acquisition

The configuration for the data processing is described below:

- Time per record: $t = 100$ ms;
- Minimum record length: $N = 200000$.

These settings have been chosen accordingly to the Nyquist-Shannon's theorem which states that, to correctly sample a signal without loss of information, the sampling frequency must be at least twice the maximum frequency present in the signal. Therefore we have a resolution of Δf:

$$\Delta f = \frac{1}{t} = 10 \text{ Hz} \tag{3.20}$$

and a sampling frequency f_c:

$$f_c = \frac{N}{t} = 2 \text{ MHz} \tag{3.21}$$

Dimensional analysis of the cantilevers was performed using a Hitachi TM3000 benchtop scanning electron microscope (SEM). SEM micrograph processing was performed using the MountainsSPIP Academic v10.0 and MountainsMap Premium v10.0 metrology software from Digital Surf.

Figure 3.15: Hitachi TM3000 benchtop SEM

As previously mentioned, the analyzed samples consisted of cantilevers with varying geometries and resonance frequencies, as well as two reference samples: a 2D grating and a segmented sample. Note that the Pelco 633 grating reference sample was calibrated in INRiM using a laser diffractometer, as reported in certificate No. 23-0686-01 issued on 2023 09-11. According to the certificate, the grating pitch along the X and Y axes is 1000 nm with an expanded uncertainty (k=2) of 0.2 nm. The measurement traceability chain starts from the measurement of the wavelength of the He-Ne laser used to illuminate the sample. The Pelco 685 piecewise reference sample was calibrated in INRiM using the metrological AFM, as reported in the certificate No. 23-0486-01 issued on 2023-06-07. The traits reported by the certificate have the following reported in the Table 3.1.

Nominal pitch [µm]	Average measured pitch [µm]	Uncertainty (k=2) [µm]
10	10,000	35
5	5,006	8
0,5	0,4998	3,0

Table 3.1: Pelco 685 grating pitch

The measurement traceability chain starts from the national standard of the meter (Winters 268), for comparison with which the laser interferometers integrated into the metrological AFM microscope for the control of the XY lateral scan were calibrated. The images of the cantilevers are measured by SEM at different magnifications, namely 200x, 250x 300x, 400x, 500x, 800x, 1000x, 1500x.

Figure 3.16 shows the SEM micrograph of the Pelco 633 reference sample, which was used to determine the pixel-to-physical-length conversion factor, using the same measurement conditions (same focus, brightness and contrast), as the ones used for measuring the cantilevers. This calibration ensures precise measurements of the cantilever dimensions, critical for the metrological characterization presented in this study.

The calibration process involves imaging the Pelco 633 reference grid (Figure 3.16) and analyzing its features to extract a profile (Figure 3.17). From this profile, the correction factor, expressed as [µm/pixel], for the X and Y axes is calculated, as summarized in Table 3.2. This ratio is then applied to convert SEM measurements of the cantilever dimensions from pixel units to micrometers. The calibration process involves imaging the Pelco 633 reference grid (Figure 3.16) and analyzing its features to extract a profile (Figure 3.17).

From this profile, two reference points are selected to ensure an accurate calibration. These points correspond to the first vertical "dark line" (labeled as point "0") and the third to last vertical "dark line" (labeled as point "1") along the extracted profile. Their positions are determined by identifying the first and penultimate local minima in the Gray Level (GL) intensity, as shown in Figure 3.17.

The distance between these two points is measured in terms of pixel units,

and their GL values are recorded to verify that the points are well-defined and distinct. The resulting measurements are summarized in Table 3.2, which reports the horizontal distance in pixels and the GL difference between the selected points.

Finally, the measured pixel distance is compared to the known physical distance between the grid lines, as specified by the Pelco 633 reference sample specifications. This comparison provides the pixel-to-physical-length conversion factor (µm/pixel), which is crucial for converting SEM measurements of cantilever dimensions from pixel units to micrometers. This precise calibration ensures that the dimensional measurements of the cantilevers, presented later in this study, are accurate and reliable.

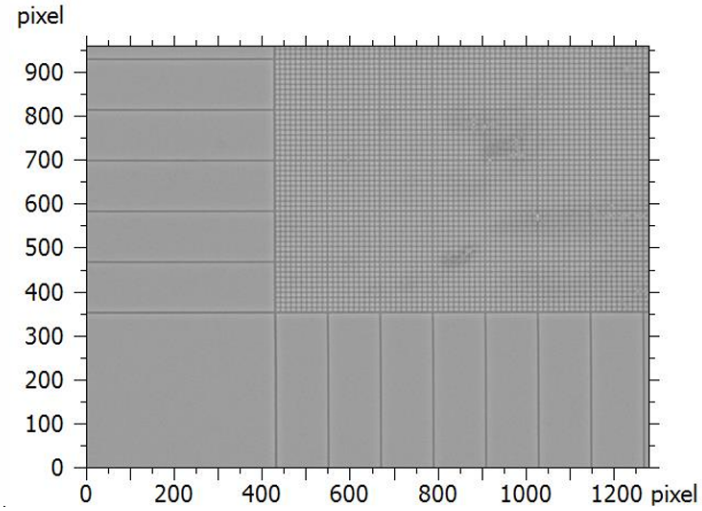

Figure 3.16: SEM micrograph of the Pelco 633 sample at 1500x magnification

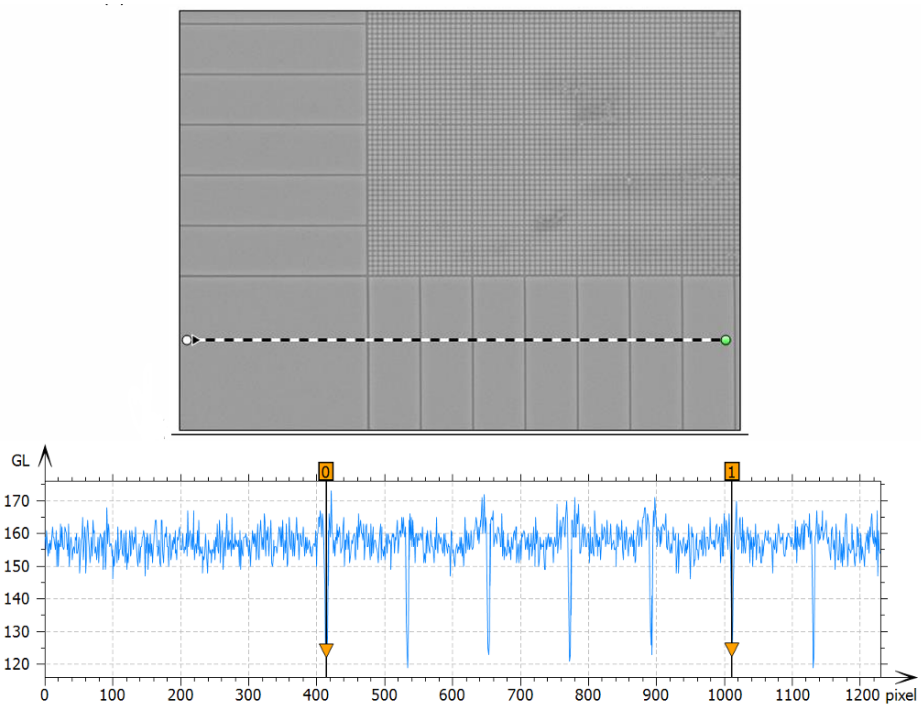

Figure 3.17: Profile extraction

Parameters	0-1	Unit
Horizontal distance	597	pixel
Height difference	0,277	GL

Table 3.2: Data from the profile extraction

It is important to underline how to calculate the various dimensions of the Bruker cantilever sample, which has the peculiarity of having a V-shaped tip.

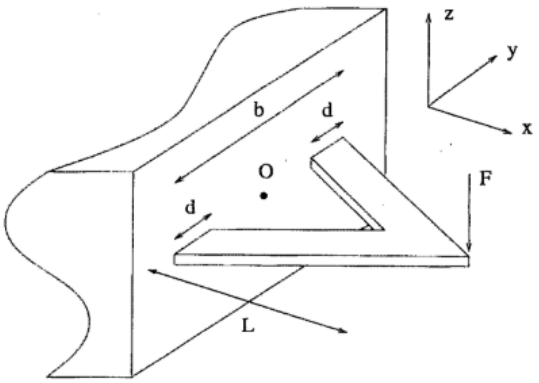

Figure 3.18: Dimensions in a V-shaped cantilever

As shown in Figure 3.18, in the case of a V-shaped cantilever, the width b

considered in the formula, d in the Figure 3.18, is calculated from the base of the cantilever rather than perpendicular to the lateral cantilever arms.

3.5 Description of the measurement

This section will discuss the process of analyzing data obtained from the measurands and measurement systems described in the previous sections.
In the first analysis, the data coming from the frequency analysis carried out by using a NI PXIe-1071 were exported directly to Excel. In Excel, the value of the resonance frequency is obtained first approximately, looking for the relative maximum by looking within the range of nominal values present in the product specifications. In particular, this is done by looking for the value of the abscissas (frequencies) corresponding to the relative maximum on the ordinates (amplitudes). To obtain an approximate experimental value of the quality factor Q, we start by dividing the value of the relative maximum of the amplitude corresponding to the resonance frequency by $\sqrt{2}$. This is also called the *-3 dB method* since going down by 3 decibels is equivalent to $10^{3/20} \simeq \sqrt{2}$, or the *half power points method* since the power dissipated in a system with viscous damping is proportional to the square of the oscillation amplitude, this implies that the points characterized by possessing half the maximum power are identified in frequency [29].

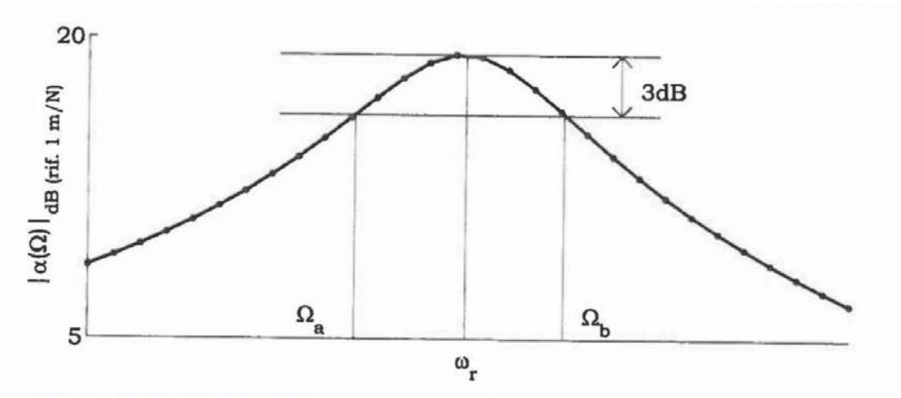

Figure 3.19: Graphical representation of the -3 dB method [29]

This single value of the amplitudes identifies two frequency values, f_1 and f_2, symmetrical with respect to the maximum, represented by the resonance frequency. We then proceed graphically by identifying among the experimental points present the one that is closest, both to the left and to the right of the peak, to the value calculated by dividing the maximum amplitude by $\sqrt{2}$, as shown in Figure 3.20. We retrieve the corresponding frequency values, which

will represent respectively f_1 (Ω_a in Figure 3.20), and f_2 (Ω_b in Figure 3.20). The quality factor Q is obtained from the following formula:

$$Q = \frac{f_R}{f_2 - f_1} \tag{3.22}$$

We then proceed using the MATLAB software to perform a fitting using the *Lorentzian curve*. The Lorentzian curve takes the shape of the peak that occurs during resonance phenomena. It is defined by the formula [30]:

$$L(x; x_0; \gamma) = \frac{1}{\pi} \cdot \frac{\gamma/2}{(x - x_0)^2 + (\gamma/2)^2} \tag{3.23}$$

where:

- x_0 is the position of the peak;
- γ is the Full Width at Half Maximum (FWHM) what measures the width of the curve;
- $L(x)$ that describes the intensity of the signal in function of x.

The MATLAB code uses the lorentzfit function which uses a derivation of the described formula. The most general version used is:

$$F(x) = \frac{p_1}{(x - p_2)^2 + p_3} + p_4 \tag{3.24}$$

where:

- p_1 controls the height of the peak and is proportional to the resonant amplitude;
- p_2 represents the central position (x_0 in the standard formula);
- p_3 proportional to the width of the curve and therefore to $\gamma/2$;
- p_4 is a constant offset.

The script then uses a 1, 2, 3 and 4 parameter version of the function.

```
function F = lfun1(p,x)
F = 1./(p.*(x.^2 + 1));
end % LFUN1

function F = lfun1c(p,x)
F = 1./(p(1).*(x.^2 + 1)) + p(2);
end % LFUN1C

function F = lfun2(p,x)
F = p(1)./(x.^2 + p(2));
end % LFUN2

function F = lfun2c(p,x)
F = p(1)./(x.^2 + p(2)) + p(3);
end % LFUN2C

function F = lfun3(p,x)
F = p(1)./((x-p(2)).^2+p(3));
end % LFUN3

function F = lfun3c(p,x)
F = p(1)./((x-p(2)).^2+p(3)) + p(4);
end % LFUN3C
```

Figure 3.20: Matlab script

This is the function that is the basis of the fitting that is used in the script. In particular, initially in the script the experimental value of the resonant frequency and quality factor obtained from the previous calculation is extracted from Excel and also all the experimental values obtained from the NI PXIe-1071. The vectors that will be used later are also now initialized. A windowing is then done on the values of frequencies (x) and amplitudes (y) taken from Excel, centered in the value of the resonance frequency calculated in the Excel file ("$f_{res,actual}$" in Figure 3.21). It will depend on an integer variable t, which can be varied depending on the peak considered. In particular, for each cantilever, the t was chosen that not only visually best fitted the curve of the raw values, the green curve in the graphs in Section 4.1, but also the one that produced the results that were closest to the experimental values mathematically obtained from the raw values. The procedure will be repeated through a while loop that thanks to an index j will create three different windowings and therefore will apply the Lorentzian fitting to the three different windowings obtained.

```
while j<4

x1=x(f_res_actual/10-j*t/(t/10)-t:f_res_actual/10+j*t/(t/10)+t);
y1=y(f_res_actual/10-j*t/(t/10)-t:f_res_actual/10+j*t/(t/10)+t);


[yprime, params, resnorm, residual] = lorentzfit(x1,y1);
```

Figure 3.21: Matlab script

We proceed by obtaining from each Lorentzian the value of the resonance frequency, the values of the frequencies at -3 dB and therefore calculating the value of the quality factor. We then calculate the average value of f_R and Q among the three obtained from the while loop and therefore the standard uncertainties associated with them. The associated standard uncertainty with uniform distribution is calculated using the following formulas:

$$u_{f_R} = \frac{f_{R,max} - f_{R,min}}{\sqrt{12}} \tag{3.25}$$

$$u_Q = \frac{Q_{max} - Q_{min}}{\sqrt{12}} \tag{3.26}$$

These results will be used as input values in a different Excel file along with the other input values:

- the dimensional parameters obtained from SEM ($b,\ L,\ \Delta L$),
- quantities related to air properties (measured temperature, relative humidity and static pressure).

The latter will specifically be used in the Rasmussen's formulas described in Section 3.1.3 and along with the width of the cantilever b and the resonant frequency f_R will be used to determine the Reynolds number $Re = \pi\ \rho_{air}\ f_R\ b^2/(2\ \mu_{air})$ and to it will be associated its combined uncertainty. These two outputs will in turn be used as input terms in a further MATLAB script in which the hydrodynamic function is calculated with the formulas outlined in Section 3.1.4. Lastly the obtained results are combined in the final Sader's formula and the propagation of uncertainties is calculated for each factor of the formula to obtain the dynamic spring constant and its combined uncertainty.

Chapter 4

Experimental results

4.1 Dynamic Results

The graphs below represent on the left the raw results obtained from the cantilever analysis and reported on Excel, focusing on the first resonance peak within the entire spectrum, on the right instead the processing of the raw data on MATLAB.

In particular, in the MATLAB graph we find four curves: the green one represents the raw data while the other three represent the three cycles of approximation with Lorentzians as explained in Section 3.5. In all the cantilevers studied in this section, the point furthest from the base of the cantilever, i.e. the tip, was considered as the investigation point, since it has a greater dynamic response and therefore clearer results are obtained.
The graphs compare the experimental data obtained from the raw results and the data obtained from the MATLAB data analysis. In particular, two phenomena can be noted from the graphs:

- Cantilevers with lower resonance frequencies 10-20 kHz, present raw data with a lower density of sampled points, which leads to lower precision in the representation of the signal and consequently the fitting of the Lorentzians will be more unstable.

- At very high frequencies (300 kHz) a background noise occurred, probably due to the instrument used or to interference or disturbances in the measurement environment or in the acquisition system, which introduced distortions in the shape of the graph. This is particularly noticeable only

in the Park tip since it has the highest resonance frequency.

4.1.1 MikroMasch CSC38 dynamic results

Tip A

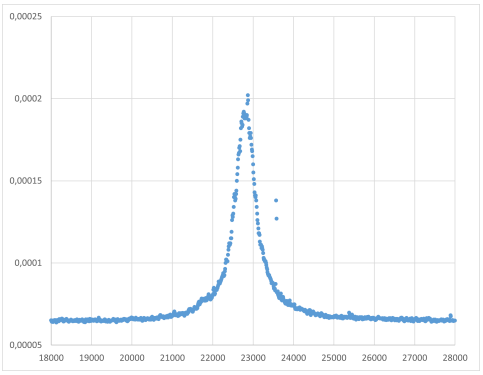

(a) Tip A CSC raw data

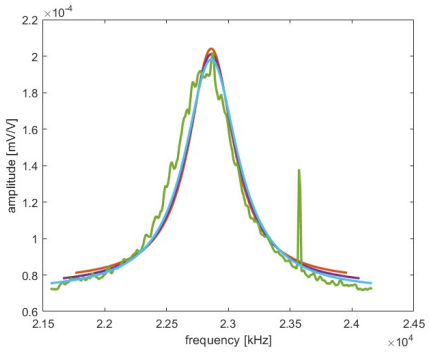

(b) Tip A CSC elaborated data

Figure 4.1: Comparison of Tip A CSC results

Parameter	Experimental	Analytical
Resonant frequency f_R	22870 Hz	22860 Hz
Quality factor Q	46,67	51,32

Table 4.1: Comparison of Tip A CSC parameters

Tip B

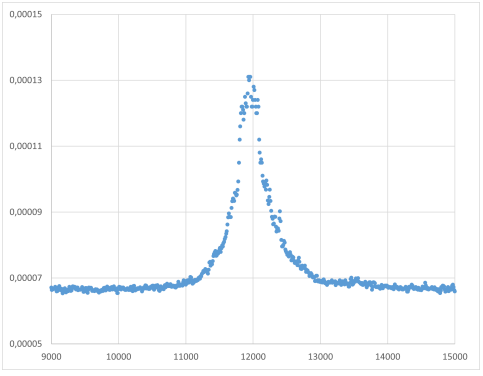

(a) Tip B CSC raw data

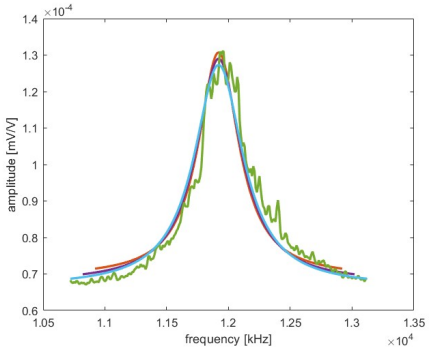

(b) Tip B CSC elaborated data

Figure 4.2: Comparison of Tip B CSC results

Parameter	Experimental	Analytical
Resonant frequency f_R	11930 Hz	11920,02 Hz
Quality factor Q	23,39	21,36

Table 4.2: Comparison of Tip B CSC parameters

Tip C

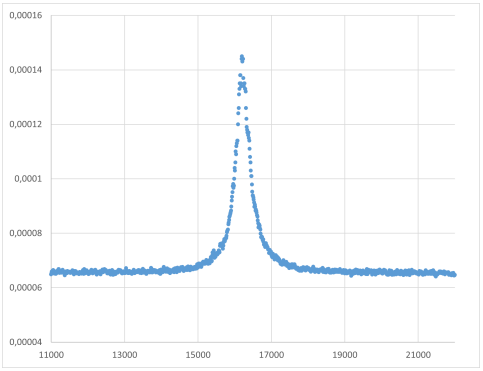

(a) Tip C CSC raw data

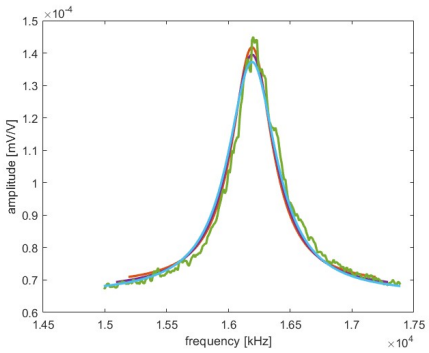

(b) Tip C CSC elaborated data

Figure 4.3: Comparison of Tip C CSC results

Parameter	Experimental	Analytical
Resonant frequency f_R	16200 Hz	16190,02 Hz
Quality factor Q	36	32,52

Table 4.3: Comparison of Tip C CSC parameters

4.1.2 MikroMasch XSC11 dynamic results

Tip A

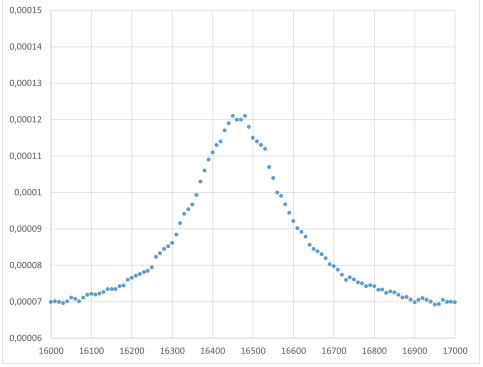

(a) Tip A XSC raw data

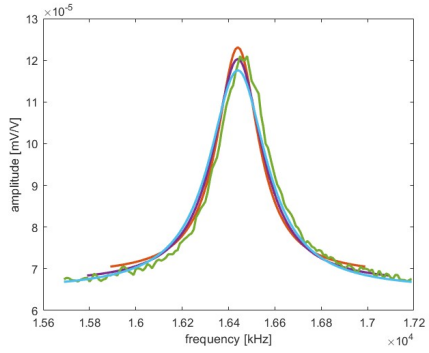

(b) Tip A XSC elaborated data

Figure 4.4: Comparison of Tip A XSC results

Parameter	Experimental	Analytical
Resonant frequency f_R	16450 Hz	16440 Hz
Quality factor Q	47	46,54

Table 4.4: Comparison of Tip A XSC parameters

Tip B

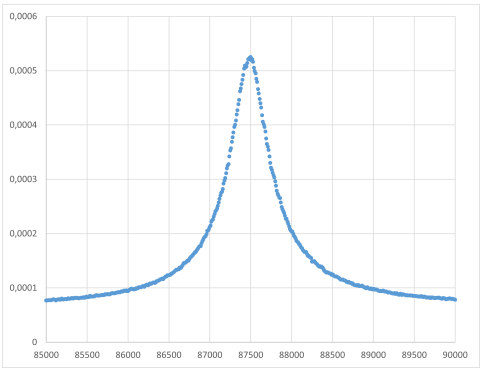

(a) Tip B XSC raw data

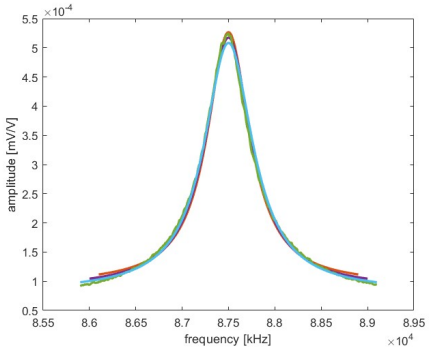

(b) Tip B XSC elaborated data

Figure 4.5: Comparison of Tip B XSC results

Parameter	Experimental	Analytical
Resonant frequency f_R	87500 Hz	87499,73 Hz
Quality factor Q	203,49	198,90

Table 4.5: Comparison of Tip B XSC parameters

4.1.3 Bruker NPG10 dynamic results

Tip A

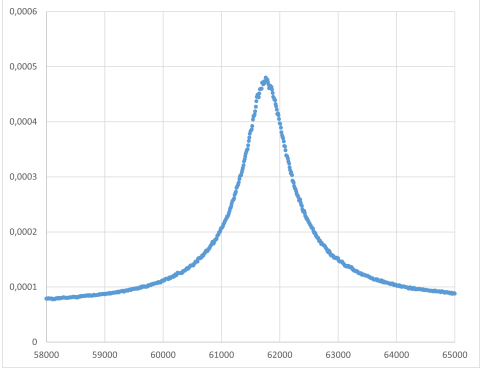

(a) Tip A Bruker raw data

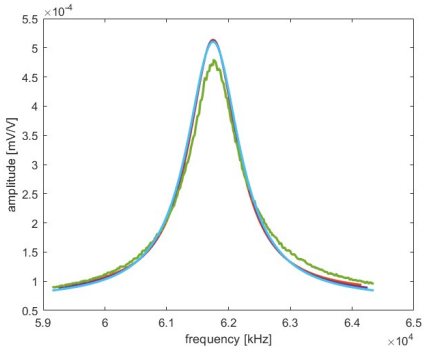

(b) Tip A Bruker elaborated data

Figure 4.6: Comparison of Tip A Bruker results

Parameter	Experimental	Analytical
Resonant frequency f_R	61760 Hz	61750,38 Hz
Quality factor Q	85,78	85,90

Table 4.6: Comparison of Tip A Bruker parameters

Tip B

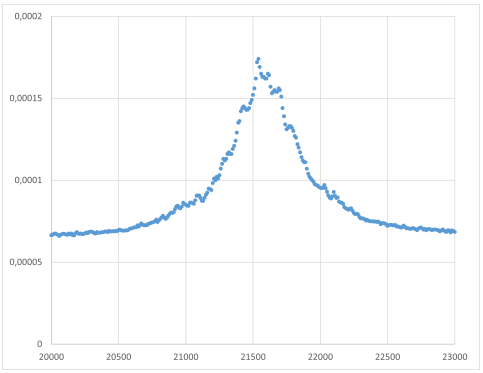

(a) Tip B Bruker raw data

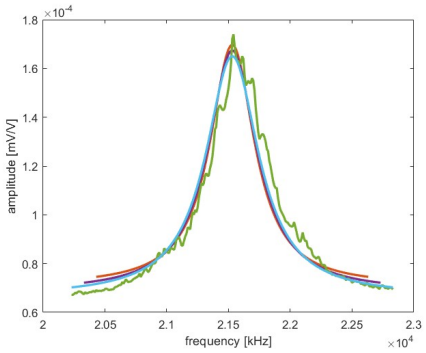

(b) Tip B Bruker elaborated data

Figure 4.7: Comparison of Tip B Bruker results

Parameter	Experimental	Analytical
Resonant frequency f_R	21540 Hz	21530,05 Hz
Quality factor Q	46,83	45,07

Table 4.7: Comparison of Tip B Bruker parameters

Tip C

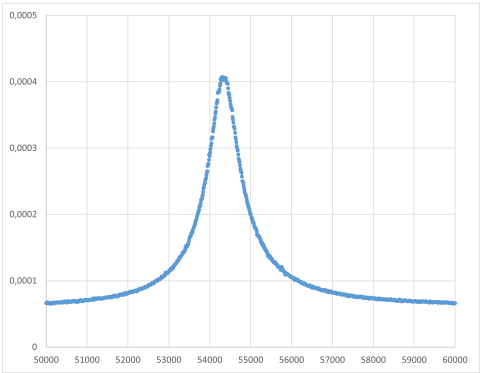

(a) Tip C Bruker raw data

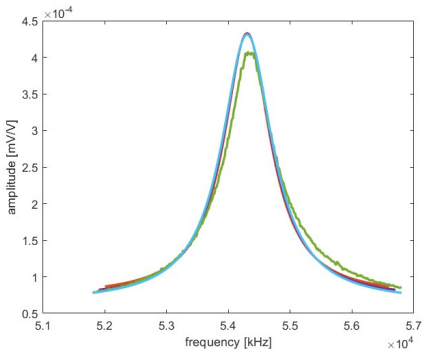

(b) Tip C Bruker elaborated data

Figure 4.8: Comparison of Tip C Bruker results

Parameter	Experimental	Analytical
Resonant frequency f_R	54310 Hz	54300,81 Hz
Quality factor Q	77,59	77,79

Table 4.8: Comparison of Tip C Bruker parameters

Tip D

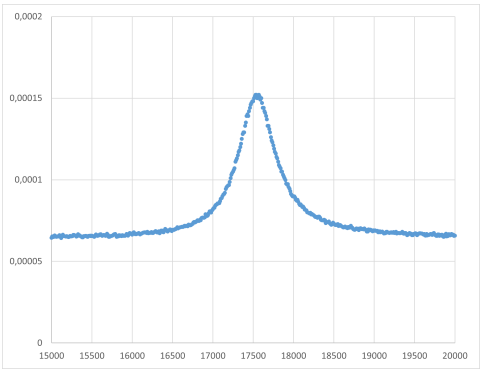

(a) Tip D Bruker raw data

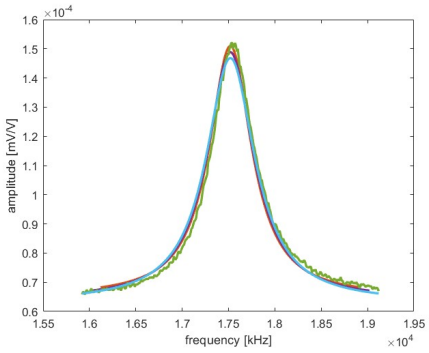

(b) Tip D Bruker elaborated data

Figure 4.9: Comparison of Tip D Bruker results

Parameter	Experimental	Analytical
Resonant frequency f_R	17530 Hz	17520,04 Hz
Quality factor Q	29,22	28,34

Table 4.9: Comparison of Tip D Bruker parameters

4.1.4 Nanosensors Atec ContAu-10 dynamic results

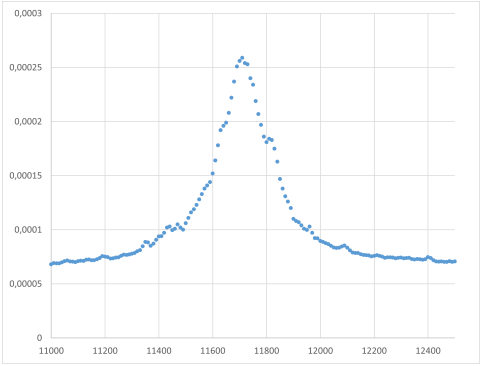

(a) Atec ContAu raw data

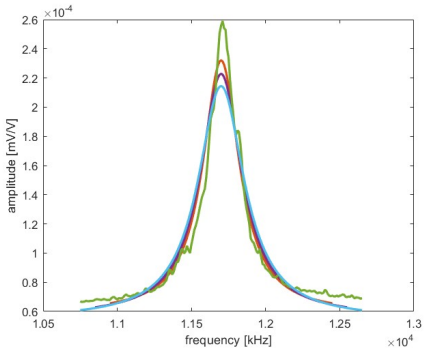

(b) Atec ContAu elaborated data

Figure 4.10: Comparison of Atec ContAu results

Parameter	Experimental	Analytical
Resonant frequency f_R	11710 Hz	11700.02 Hz
Quality factor Q	55,76	43,19

Table 4.10: Comparison of Atec ContAu parameters

4.1.5 Olympus Biolever dynamic results

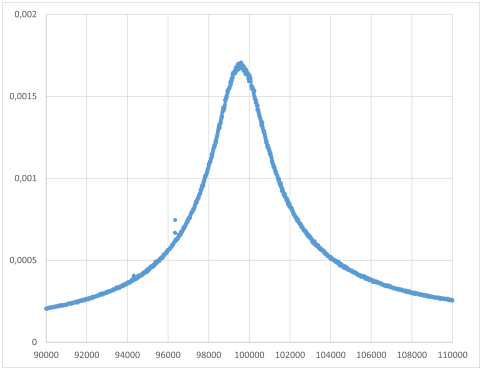

(a) Biolever raw data

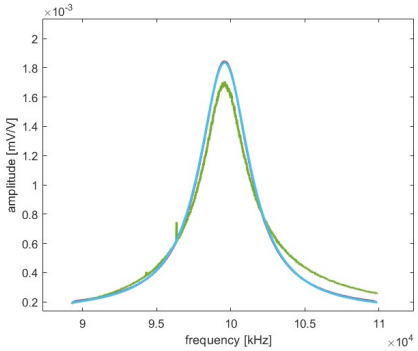

(b) Biolever elaborated data

Figure 4.11: Comparison of Biolever results

Parameter	Experimental	Analytical
Resonant frequency f_R	99590 Hz	99584.52 Hz
Quality factor Q	38,45	35,94

Table 4.11: Comparison of Biolever parameters

4.1.6 ParkSystems PPP NCHR dynamic results

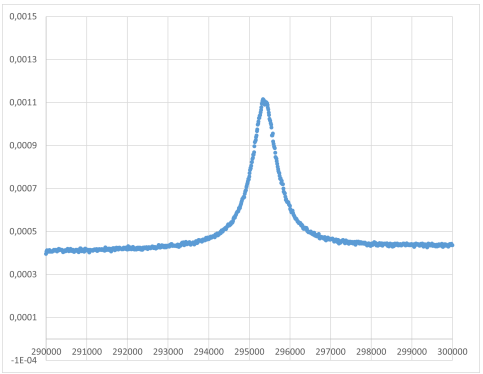

(a) Park Cantilever raw data

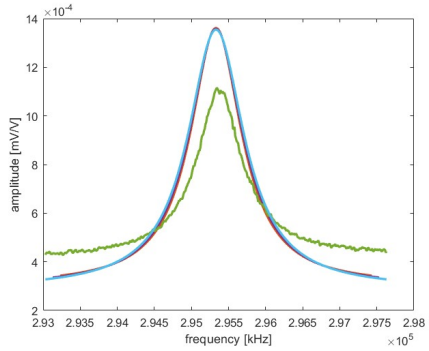

(b) Park Cantilever elaborated data

Figure 4.12: Comparison of Park Cantilever results

Parameter	Experimental	Analytical
Resonant frequency f_R	295340 Hz	295330.80 Hz
Quality factor Q	434,32	435,58

Table 4.12: Comparison of Park Cantilever parameters

4.1.7 Standard uncertainty for resonant frequency and quality factor

As described in Section 3.5, the results of the three Lorentzian curves are used to obtain the values of the standard uncertainty of the resonance frequency u_{f_R} and of the quality factor u_Q.

For the resonance frequencies f_R the uncertainties $u(f_R)$ assume very small values for all cantilevers, thus indicating a high precision in the determination of the latter.

The uncertainties of the quality factor Q, $u(Q)$, are generally higher since it is more difficult to obtain high precision and repeatability. This difference is given by the fact that Q varies more with respect to the fitting that is chosen.

Cantilever	$u(f_R)$	$u(Q)$
Atec ContAu	0,0033	2,81
MikroMasch CSC38		
Cantilever A	0,0078	1,965
Cantilever B	0,00235	0,88
Cantilever C	0,0022	1,505
Bruker NPG10		
Cantilever A	0,0040	1,38
Cantilever B	0,0061	2,17
Cantilever C	0,0067	1,285
Cantilever D	0,00376	1,057
MikroMasch XSC11		
Cantilever A	0,00059	4,52
Cantilever B	0,0235	5,24
Olympus Biolever	0,0288	0,15
ParkSystems PPP NCHR	0,0031	7,41

Table 4.13: Results of uncertainties for resonant frequency and quality factor

It can be noted that, for all the analyzed tips, the standard uncertainty associated with the resonance frequency is smaller than the resolution itself, where the chosen resolution of NI PXIe-107 is $\Delta f = 10$ Hz.

In these particular cases, the value of the resolution represents the associated standard uncertainty, as it is determined by the parameters used for the data processing, specifically $\Delta f = 1/T$, where T is the measurement duration. This indicates that the resolution is not an intrinsic limit of the instrument, but rather a function of the measurement time.

4.2 Dimensional results

The length L, the cantilever tip-tip distance ΔL and the width b in pixels have been extracted by analyzing the cantilecer images obtained with the scanning electron microscope. Note that the standard deviation of L, ΔL and b is calculated because multiple width and length profiles were extracted, as reported in Figure 4.13 and Figure 4.14.

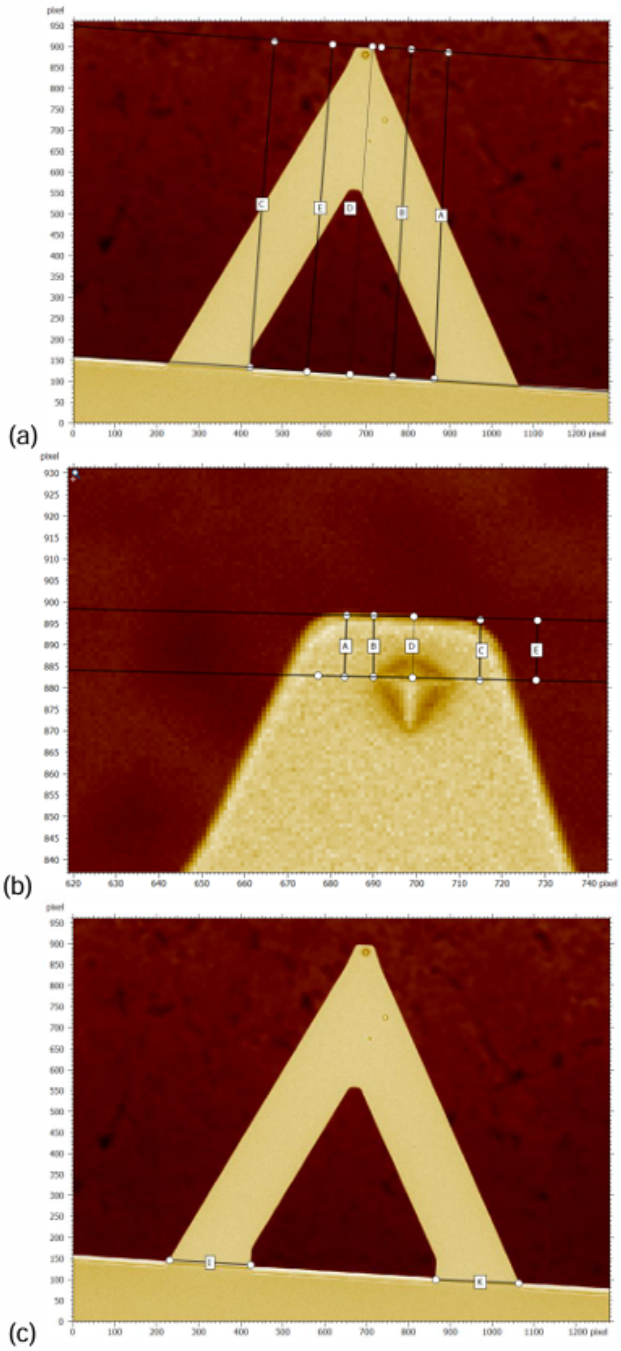

Figure 4.13: Extraction of dimensional parameters (a) length L, (b) length ΔL and (c) width b for Bruker NPG V-shape cantilevers

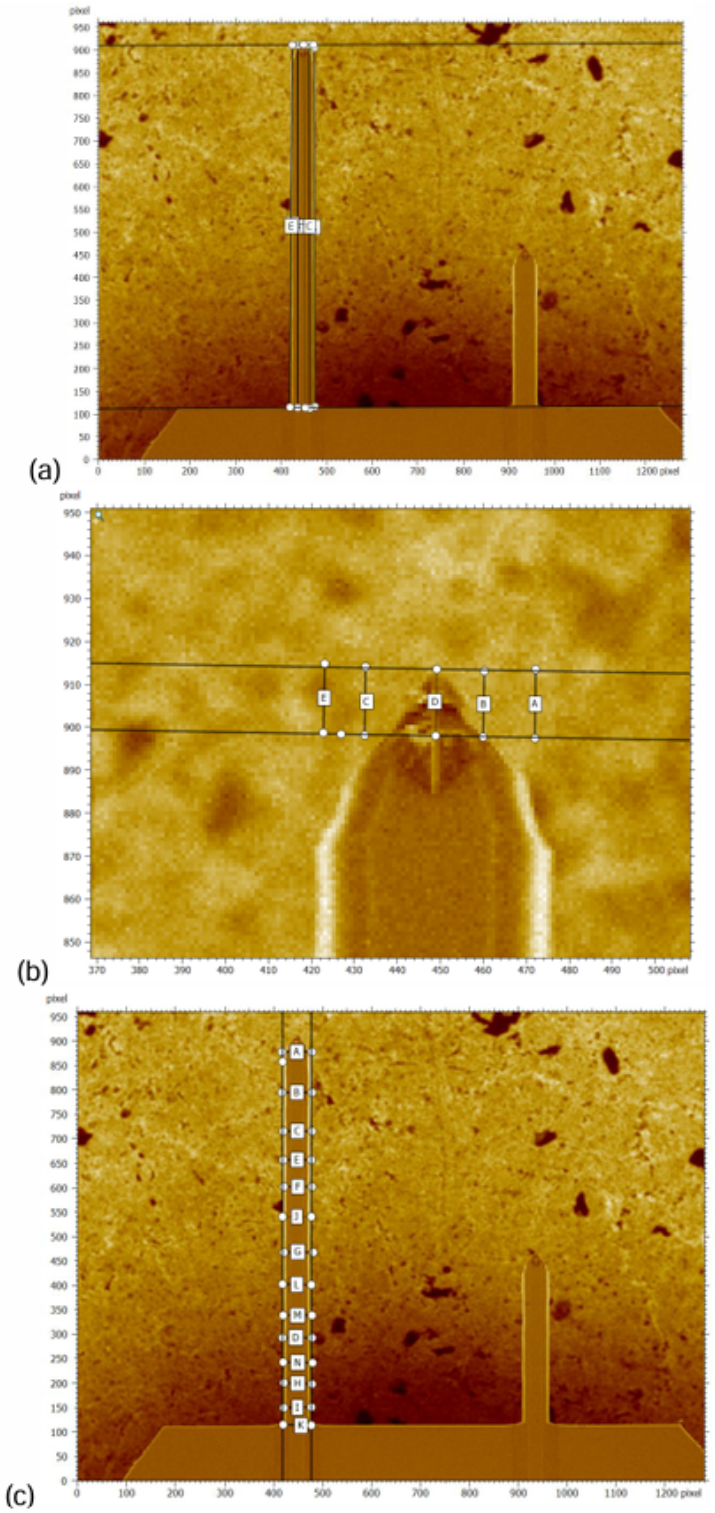

Figure 4.14: Extraction of dimensional parameters (a) length L, (b) length ΔL and (c) width b for rectangular MikroMasch XSC11 cantilevers

Using the coefficients [µm/pixel] from the reference samples calibrated as explained in Section 3.4, the length L, the length ΔL and the width b in µm were calculated. The results of the dimensional measurements carried out on

the cantilevers and referred to the International System (SI) are reported in Table 4.25.

Cantilever	L [µm]	$\sigma(L)$ [µm]	ΔL [µm]	$\sigma\ (\Delta L)$ [µm]	b [µm]	$\sigma(b)$ [µm]
Atec ContAu	455,46	1,31	-	-	51,44	1,00
MikroMasch CSC38						
Cantilever A	266,30	1,00	15,03	0,25	35,76	0,97
Cantilever B	366,97	1,21	15,38	0,16	35,75	0,96
Cantilever C	316,55	1,44	15,47	0,07	35,75	0,96
Bruker NPG10						
Cantilever A	115,44	0,41	3,85	0,12	30,88	0,01
Cantilever B	203,99	0,56	3,69	0,05	48,91	0,53
Cantilever C	115,03	0,43	3,66	0,14	24,97	0,79
Cantilever D	203,16	0,82	4,10	0,09	29,14	0,18
MikroMasch XSC11						
Cantilever A	521,50	2,88	10,32	0,22	36,72	0,96
Cantilever B	230,63	1,56	10,62	0,26	34,67	1,16
Olympus Biolever	41,40	0,06	3,87	0,06	17,49	0,13
ParkSystems PPP NCHR	133,96	0,33	12,14	0,29	38,16	0,83

Table 4.14: Results of dimensional measurements carried out on the various cantilevers and referred to the SI

In the case of the Atec ContAu it was not possible to obtain ΔL and its related uncertainty and therefore it will not be possible to calculate the effective value of the spring constant.

4.3 Hydrodynamic function and Rasmussen's model results

Table 4.15 represent the measurements of the atmospheric static pressure p_s, temperature T and relative humidity RH. These parameters were recorded at the time of measurement of each analyzed cantilever. It should also be highlighted that the standard uncertainties associated with temperature T, pressure p_s and humidity RH are of type B, and therefore depend on the accuracy of the instrument used for the measurements. The latter are therefore the same for all cantilevers, as they derive from the metrological characterization of the measuring instruments and not from the specific characteristics of the cantilevers themselves. In particular, the uncertainty on the temperature is equal to 0.1°C, on the pressure is 50 Pa, while the uncertainty on the relative humidity is set to 10% of its measured value.

Cantilever	p_s [Pa]	T [∘C]	RH [%]
Atec ContAu	98200	23,6	52,5
MikroMasch CSC38			
Cantilever A	97900	23,7	52,9
Cantilever B	97900	23,7	52,9
Cantilever C	97900	23,7	52,9
Bruker NPG10			
Cantilever A	97900	23,7	52,9
Cantilever B	97900	23,7	52,9
Cantilever C	99800	24	52,9
Cantilever D	99800	24	52,9
MikroMasch XSC11			
Cantilever A	98000	23,8	49,9
Cantilever B	98000	23,8	49,9
Olympus Biolever	97900	23,8	49,8
ParkSystems PPP NCHR	98000	23,8	49,9

Table 4.15: Environmental conditions (Pressure, Temperature and Humidity) measured for different cantilevers

Table 4.16 shows the results of the physical properties of air and the associated combined uncertainties, calculated for different cantilevers using the Rasmussen model. The columns show the values of the air density (ρ_{air}), with the respective combined uncertainty ($u(\rho_{air})$), and of the dynamic vis-

cosity of air (μ_{air}), with the associated uncertainty ($u(\mu_{air})$) for each analyzed cantilever. The combined uncertainties of these results, as suggested by the used formulas, arise both from uncertainties due to the measuring instruments of static pressure, relative humidity and temperature, and from calculation uncertainties arising from the Rasmussen model.

Cantilever	ρ_{air} [kg/m^3]	$u(\rho_{air})$	μ_{air} [Pa · s]	$u(\mu_{air})$
Atec ContAu	1,15	$5,6 \cdot 10^{-4}$	$1,83 \cdot 10^{-5}$	$3,2 \cdot 10^{-9}$
MikroMasch CSC38				
Cantilever A	1,14	$5,7 \cdot 10^{-4}$	$1,83 \cdot 10^{-5}$	$3,2 \cdot 10^{-9}$
Cantilever B	1,14	$5,7 \cdot 10^{-4}$	$1,83 \cdot 10^{-5}$	$3,2 \cdot 10^{-9}$
Cantilever C	1,14	$5,7 \cdot 10^{-4}$	$1,83 \cdot 10^{-5}$	$3,2 \cdot 10^{-9}$
Bruker NPG10				
Cantilever A	1,14	$5,7 \cdot 10^{-4}$	$1,83 \cdot 10^{-5}$	$3,2 \cdot 10^{-9}$
Cantilever B	1,14	$5,7 \cdot 10^{-4}$	$1,83 \cdot 10^{-5}$	$3,2 \cdot 10^{-9}$
Cantilever C	1,16	$5,7 \cdot 10^{-4}$	$1,83 \cdot 10^{-5}$	$3,2 \cdot 10^{-9}$
Cantilever D	1,16	$5,7 \cdot 10^{-4}$	$1,83 \cdot 10^{-5}$	$3,2 \cdot 10^{-9}$
MikroMasch XSC11				
Cantilever A	1,14	$5,5 \cdot 10^{-4}$	$1,83 \cdot 10^{-5}$	$3,2 \cdot 10^{-9}$
Cantilever B	1,14	$5,5 \cdot 10^{-4}$	$1,83 \cdot 10^{-5}$	$3,2 \cdot 10^{-9}$
Olympus Biolever	1,14	$5,5 \cdot 10^{-4}$	$1,83 \cdot 10^{-5}$	$3,2 \cdot 10^{-9}$
ParkSystems PPP NCHR	1,14	$5,5 \cdot 10^{-4}$	$1,83 \cdot 10^{-5}$	$3,2 \cdot 10^{-9}$

Table 4.16: Air properties results and their standard uncertainty for different cantilevers

The uncertainties of the experimental parameter are then exploited to evaluate the uncertainty of the Reynold's number, and consequently, to propagate the uncertainties into the imaginary part of the hydrodynamic function for the rectangular beams, calculated according to the equations in Section 3.1.4. Values are reported in Table 4.17.

Cantilever	Re	$u(Re)$	$\Gamma_{i,rect}(\omega)$	$u(\Gamma_{i,rect})$
Atec ContAu	3,05	0,12	2,12	$3.162 \cdot 10^{-1}$
MikroMasch CSC38				
Cantilever A	2,87	0,16	2,195	$1.21 \cdot 10^{-2}$
Cantilever B	1,49	0,08	3,27	$3.19 \cdot 10^{-2}$
Cantilever C	2,03	0,11	2,71	$3.43 \cdot 10^{-2}$
Bruker NPG10				
Cantilever A	5,775	0,005	1,455	$4.79 \cdot 10^{-3}$
Cantilever B	5,05	0,11	1,57	$7.28 \cdot 10^{-3}$
Cantilever C	3,38	0,21	1,455	$4.79 \cdot 10^{-3}$
Cantilever D	1,485	0,018	1,57	$2.34 \cdot 10^{-3}$
MikroMasch XSC11				
Cantilever A	2,18	0,114	2,59	$1.05 \cdot 10^{-2}$
Cantilever B	11,58	0,73	0,98	$2.69 \cdot 10^{-2}$
Olympus Biolever	2,99	0,044	2,14	$9.43 \cdot 10^{-4}$
ParkSystems PPP NCHR	42,21	1,84	0,48	$6.71 \cdot 10^{-2}$

Table 4.17: Reynold's number and imaginary part of the hydrodynamic function results and standard uncertainties

4.4 Uncertainties' propagation

Considering the two final formulas that serve to derive the dynamic elastic constant k and the effective elastic constant k_{eff} (3.10) (3.11), the standard uncertainties and therefore the variances of each parameter of the equations are reported in the following tables for each cantilever.
The table is divided into three columns:

- the first ($u^2(x_i)$) reports the uncertainties associated with the input parameters,
- the second ($\frac{\partial k_{eff}}{\partial x_i}$) lists the partial derivatives of the parameter k_{eff} with respect to the input parameters,
- the third ($u^2(y)$) represents the total contribution of each parameter to the combined uncertainty on the final result.

An *uncertainty budget* serves to evaluate the sources of uncertainty and quantify among the parameters that most contribute to the final composite uncertainty.
This gives an idea of the accuracy and reliability of the results both as individual contributions and on the final result.

The uncertainties related to the parameters in the Sader formula that contribute to the uncertainty of k were analyzed first, followed by the uncertainties associated with the parameters used to calculate k_{eff}.

Note that the total contribution of the uncertainty on k is then propagated as associated uncertainty as an input parameter in the second formula, and that the associated uncertainty of L is the same in the two formulas, but the total contribution changes because its partial derivative with respect to the output parameter changes.

4.4.1 MikroMasch CSC38 uncertainty budget

Tip A

Parameter	$u^2(x_i)$	$\left(\frac{\partial k_S}{\partial x_i}\right)$	$u_c^2(y)$
b	$9,4 \cdot 10^{-13}$	$9,6 \cdot 10^{3}$	$8,7 \cdot 10^{-5}$
L	$1,0 \cdot 10^{-12}$	$6,5 \cdot 10^{2}$	$4,2 \cdot 10^{-7}$
ρ_{air}	$3,2 \cdot 10^{-7}$	$1,5 \cdot 10^{-1}$	$7,3 \cdot 10^{-9}$
f_R	$1,0 \cdot 10^{2}$	$1,5 \cdot 10^{-5}$	$2,3 \cdot 10^{-8}$
Q	$3,9$	$3,4 \cdot 10^{-3}$	$4,4 \cdot 10^{-5}$
Γ_i	$1,47 \cdot 10^{-4}$	$7,9 \cdot 10^{-2}$	$9,0 \cdot 10^{-7}$
k			$1,3 \cdot 10^{-4}$
k	$1,3 \cdot 10^{-4}$	$1,2$	$1,9 \cdot 10^{-4}$
L	$1,0 \cdot 10^{-12}$	$-1,4 \cdot 10^{+2}$	$1,9 \cdot 10^{-8}$
ΔL	$6,3 \cdot 10^{-14}$	$2,4 \cdot 10^{+3}$	$3,8 \cdot 10^{-7}$
k_{eff}			$1,9 \cdot 10^{-4}$

Table 4.18: Results of uncertainty Budget for Cantilever A (CSC)

Tip B

Parameter	$u^2(x_i)$	$\left(\frac{\partial k_S}{\partial x_i}\right)$	$u_c^2(y)$
b	$9,4 \cdot 10^{-13}$	$2,2 \cdot 10^{3}$	$4,7 \cdot 10^{-6}$
L	$1,5 \cdot 10^{-12}$	$1,1 \cdot 10^{2}$	$1,7 \cdot 10^{-8}$
ρ_{air}	$3,2 \cdot 10^{-7}$	$3,5 \cdot 10^{-2}$	$3,9 \cdot 10^{-10}$
f_R	$1,0 \cdot 10^{2}$	$6,7 \cdot 10^{-6}$	$4,5 \cdot 10^{-9}$
Q	$7,8 \cdot 10^{-1}$	$1,9 \cdot 10^{-3}$	$2,7 \cdot 10^{-6}$
Γ_i	$1,02 \cdot 10^{-4}$	$1,2 \cdot 10^{-2}$	$1,5 \cdot 10^{-8}$
k			$7,5 \cdot 10^{-6}$
k	$7,5 \cdot 10^{-6}$	$1,1 \cdot 10^{+0}$	$9,7 \cdot 10^{-6}$
L	$1,5 \cdot 10^{-12}$	$-1,6 \cdot 10^{+1}$	$3,9 \cdot 10^{-10}$
ΔL	$2,6 \cdot 10^{-14}$	$3,9 \cdot 10^{+2}$	$3,9 \cdot 10^{-9}$
k_{eff}			$9,7 \cdot 10^{-6}$

Table 4.19: Results of uncertainty Budget for Cantilever B (CSC)

Tip C

Parameter	$u^2(x_i)$	$\left(\frac{\partial k_S}{\partial x_i}\right)$	$u_c^2(y)$
b	$9,2 \cdot 10^{-13}$	$4,5 \cdot 10^{3}$	$1,9 \cdot 10^{-5}$
L	$2,1 \cdot 10^{-12}$	$2,5 \cdot 10^{2}$	$1,3 \cdot 10^{-7}$
ρ_{air}	$3,2 \cdot 10^{-7}$	$7,0 \cdot 10^{-2}$	$1,6 \cdot 10^{-9}$
f_R	$1,0 \cdot 10^{2}$	$9,9 \cdot 10^{-6}$	$9,8 \cdot 10^{-9}$
Q	$2,3 \cdot 10^{0}$	$2,5 \cdot 10^{-3}$	$1,4 \cdot 10^{-5}$
Γ_i	$1,18 \cdot 10^{-4}$	$3,0 \cdot 10^{-2}$	$1,0 \cdot 10^{-7}$
k			$3,3 \cdot 10^{-5}$
k	$3,3 \cdot 10^{-5}$	$1,2 \cdot 10^{+0}$	$4,4 \cdot 10^{-5}$
L	$2,1 \cdot 10^{-12}$	$-4,5 \cdot 10^{+1}$	$4,3 \cdot 10^{-9}$
ΔL	$4,9 \cdot 10^{-15}$	$9,3 \cdot 10^{+2}$	$4,2 \cdot 10^{-9}$
k_{eff}			$4,4 \cdot 10^{-5}$

Table 4.20: Results of uncertainty Budget for Cantilever C (CSC)

4.4.2 MikroMasch XSC11 uncertainty budget

Parameter	Cantilever A			Cantilever B		
	$u^2(x_i)$	$\left(\frac{\partial k_S}{\partial x_i}\right)$	$u_c^2(y)$	$u^2(x_i)$	$\left(\frac{\partial k_S}{\partial x_i}\right)$	$u_c^2(y)$
b	$9,2 \cdot 10^{-13}$	$1,1 \cdot 10^{4}$	$1,1 \cdot 10^{-4}$	$1,3 \cdot 10^{-12}$	$2,2 \cdot 10^{5}$	$6,3 \cdot 10^{-2}$
L	$8,3 \cdot 10^{-12}$	$3,8 \cdot 10^{2}$	$1,2 \cdot 10^{-6}$	$2,4 \cdot 10^{-12}$	$1,7 \cdot 10^{4}$	$7,2 \cdot 10^{-4}$
ρ_{air}	$3,1 \cdot 10^{-7}$	$1,7 \cdot 10^{-1}$	$9,1 \cdot 10^{-9}$	$3,1 \cdot 10^{-7}$	$3,5$	$3,7 \cdot 10^{-6}$
f_R	$1,0 \cdot 10^{2}$	$2,4 \cdot 10^{-5}$	$5,8 \cdot 10^{-8}$	$1,0 \cdot 10^{2}$	$9,1 \cdot 10^{-5}$	$8,3 \cdot 10^{-7}$
Q	$2,0 \cdot 10^{1}$	$4,2 \cdot 10^{-3}$	$3,7 \cdot 10^{-4}$	$2,7 \cdot 10^{1}$	$2,0 \cdot 10^{-2}$	$1,1 \cdot 10^{-2}$
$\Gamma_{i,rect}(\omega)$	$1,1 \cdot 10^{-4}$	$7,6 \cdot 10^{-2}$	$6,4 \cdot 10^{-7}$	$7,21 \cdot 10^{-4}$	$4,1$	$1,2 \cdot 10^{-2}$
k			$4,8 \cdot 10^{-4}$			$8,7 \cdot 10^{-2}$
k	$4,8 \cdot 10^{-4}$	$1,1$	$5,4 \cdot 10^{-4}$	$8,7 \cdot 10^{-2}$	$1,1$	$1,1 \cdot 10^{-1}$
L	$8,3 \cdot 10^{-12}$	$-2,4 \cdot 10^{1}$	$4,9 \cdot 10^{-9}$	$2,4 \cdot 10^{-12}$	$-2,8 \cdot 10^{3}$	$1,9 \cdot 10^{-5}$
ΔL	$4,8 \cdot 10^{-14}$	$1,2 \cdot 10^{3}$	$7,3 \cdot 10^{-8}$	$4,8 \cdot 10^{-14}$	$6,2 \cdot 10^{4}$	$1,9 \cdot 10^{-4}$
k_{eff}			$5,4 \cdot 10^{-4}$			$1,1 \cdot 10^{-1}$

Table 4.21: Results of uncertainty budget MikroMasch XSC11

4.4.3 Bruker NPG10 uncertainty budget

Parameter	Cantilever A			Cantilever B		
	$u^2(x_i)$	$\left(\frac{\partial k_S}{\partial x_i}\right)$	$u_c^2(y)$	$u^2(x_i)$	$\left(\frac{\partial k_S}{\partial x_i}\right)$	$u_c^2(y)$
b	$1.0 \cdot 10^{-16}$	$2.9 \cdot 10^{4}$	$8.5 \cdot 10^{-8}$	$2.8 \cdot 10^{-13}$	$5.6 \cdot 10^{3}$	$8.9 \cdot 10^{-6}$
L	$1.7 \cdot 10^{-13}$	$3.9 \cdot 10^{3}$	$2.6 \cdot 10^{-6}$	$3.1 \cdot 10^{-13}$	$6.8 \cdot 10^{2}$	$1.4 \cdot 10^{-7}$
ρ_{air}	$3.2 \cdot 10^{-7}$	$3.9 \cdot 10^{-1}$	$5.0 \cdot 10^{-8}$	$3.2 \cdot 10^{-7}$	$1.2 \cdot 10^{-1}$	$4.7 \cdot 10^{-9}$
f_R	$1.0 \cdot 10^{2}$	$1.5 \cdot 10^{-1}$	$2.1 \cdot 10^{-8}$	$1.0 \cdot 10^{2}$	$1.3 \cdot 10^{-5}$	$1.6 \cdot 10^{-8}$
Q	1.9	$5.2 \cdot 10^{-3}$	$5.2 \cdot 10^{-5}$	4.7	$3.1 \cdot 10^{-3}$	$4.4 \cdot 10^{-5}$
$\Gamma_{i,rect}(\omega)$	$2.3 \cdot 10^{-5}$	$3.1 \cdot 10^{-1}$	$2.2 \cdot 10^{-6}$	$5.48 \cdot 10^{-6}$	$8.8 \cdot 10^{-2}$	$4.2 \cdot 10^{-8}$
k			$5.7 \cdot 10^{-5}$			$5,3 \cdot 10^{-5}$
k	$5,7 \cdot 10^{-5}$	$1,1 \cdot 10^{+0}$	$7,0 \cdot 10^{-5}$	$5,3 \cdot 10^{-5}$	$1,1 \cdot 10^{+0}$	$5,9 \cdot 10^{-5}$
L	$1,7 \cdot 10^{-13}$	$-4,5 \cdot 10^{+2}$	$3,4 \cdot 10^{-8}$	$3,1 \cdot 10^{-13}$	$-3,9 \cdot 10^{+1}$	$4,9 \cdot 10^{-10}$
ΔL	$1,4 \cdot 10^{-14}$	$1,3 \cdot 10^{+4}$	$2,6 \cdot 10^{-6}$	$2,5 \cdot 10^{-15}$	$2,2 \cdot 10^{+3}$	$1,2 \cdot 10^{-8}$
k_{eff}			$7,3 \cdot 10^{-5}$			$5,9 \cdot 10^{-5}$

Parameter	Cantilever C			Cantilever D		
	$u^2(x_i)$	$\left(\frac{\partial k_S}{\partial x_i}\right)$	$u_c^2(y)$	$u^2(x_i)$	$\left(\frac{\partial k_S}{\partial x_i}\right)$	$u_c^2(y)$
b	$6,2 \cdot 10^{-13}$	$1,7 \cdot 10^{4}$	$1,8 \cdot 10^{-4}$	$3,2 \cdot 10^{-14}$	$1,4 \cdot 10^{3}$	$6,5 \cdot 10^{-8}$
L	$1,8 \cdot 10^{-13}$	$1,8 \cdot 10^{3}$	$6,1 \cdot 10^{-7}$	$6,7 \cdot 10^{-13}$	$1,0 \cdot 10^{2}$	$7,0 \cdot 10^{-9}$
ρ_{air}	$3,3 \cdot 10^{-7}$	$1,8 \cdot 10^{-1}$	$1,1 \cdot 10^{-8}$	$3,3 \cdot 10^{-7}$	$1,8 \cdot 10^{-2}$	$1,0 \cdot 10^{-10}$
f_R	$1,0 \cdot 10^{2}$	$7,7 \cdot 10^{-6}$	$6,0 \cdot 10^{-9}$	$1,0 \cdot 10^{2}$	$2,4 \cdot 10^{-6}$	$5,6 \cdot 10^{-10}$
Q	1,7	$2,7 \cdot 10^{-3}$	$1,2 \cdot 10^{-5}$	1,1	$7,3 \cdot 10^{-4}$	$5,95 \cdot 10^{-7}$
$\Gamma_{i,rect}(\omega)$	$2,3 \cdot 10^{-5}$	$1,4 \cdot 10^{-1}$	$4,8 \cdot 10^{-7}$	$5,48 \cdot 10^{-6}$	$1,3 \cdot 10^{-2}$	$9,5 \cdot 10^{-10}$
k			$1,9 \cdot 10^{-4}$			$6,7 \cdot 10^{-7}$
k	$1,9 \cdot 10^{-4}$	1,1	$2,3 \cdot 10^{-4}$	$6,7 \cdot 10^{-7}$	1,1	$7,5 \cdot 10^{-7}$
L	$1,8 \cdot 10^{-13}$	$-2 \cdot 10^{2}$	$7,2 \cdot 10^{-9}$	$6,7 \cdot 10^{-13}$	$-6,7$	$3,0 \cdot 10^{-11}$
ΔL	$2 \cdot 10^{-14}$	$6,2 \cdot 10^{3}$	$7,6 \cdot 10^{-7}$	$8,1 \cdot 10^{-15}$	$3,3 \cdot 10^{2}$	$8,9 \cdot 10^{-10}$
k_{eff}			$2,3 \cdot 10^{-4}$			$7,5 \cdot 10^{-7}$

Table 4.22: Results of uncertainty budget Bruker NPG10

4.4.4 Nanosensors Atec ContAu-10 uncertainty budget

Parameter	$u^2(x_i)$	$\left(\frac{\partial k_S}{\partial x_i}\right)$	$u_c^2(y)$
b	$1.0 \cdot 10^{-12}$	$5.1 \cdot 10^{+3}$	$2.6 \cdot 10^{-5}$
L	$1.7 \cdot 10^{-12}$	$2.9 \cdot 10^{+2}$	$1.4 \cdot 10^{-7}$
ρ_{air}	$3.2 \cdot 10^{-7}$	$1.1 \cdot 10^{-1}$	$4.1 \cdot 10^{-9}$
f_R	$1.0 \cdot 10^{+2}$	$2.2 \cdot 10^{-5}$	$4.9 \cdot 10^{-8}$
Q	$7.9 \cdot 10^{+0}$	$3.0 \cdot 10^{-3}$	$7.2 \cdot 10^{-5}$
$\Gamma_{i,rect}(\omega)$	$2.9 \cdot 10^{-3}$	$6.1 \cdot 10^{-2}$	$1.1 \cdot 10^{-5}$
k			$1.1 \cdot 10^{-4}$

Table 4.23: Results of uncertainty budget Atec ContAu

4.4.5 Olympus Biolever uncertainty budget

Parameter	$u^2(x_i)$	$\left(\frac{\partial k_S}{\partial x_i}\right)$	$u_c^2(y)$
b	$1,7 \cdot 10^{-14}$	$9,5 \cdot 10^{+3}$	$1,5 \cdot 10^{-6}$
L	$3,6 \cdot 10^{-15}$	$2,0 \cdot 10^{+3}$	$1,5 \cdot 10^{-8}$
ρ_{air}	$3,1 \cdot 10^{-7}$	$7,3 \cdot 10^{-2}$	$1,6 \cdot 10^{-9}$
f_R	$1,0 \cdot 10^{+2}$	$1,7 \cdot 10^{-6}$	$2,8 \cdot 10^{-10}$
Q	$2,2 \cdot 10^{-2}$	$2,3 \cdot 10^{-3}$	$1,2 \cdot 10^{-7}$
$\Gamma_{i,rect}(\omega)$	$8,87 \cdot 10^{-7}$	$3,9 \cdot 10^{-2}$	$1,3 \cdot 10^{-9}$
k			$1,7 \cdot 10^{-6}$
k	$1,7 \cdot 10^{-6}$	$1,3 \cdot 10^{+0}$	$3,0 \cdot 10^{-6}$
L	$3,6 \cdot 10^{-15}$	$-8,3 \cdot 10^{+2}$	$2,5 \cdot 10^{-9}$
ΔL	$3,6 \cdot 10^{-15}$	$8,9 \cdot 10^{+3}$	$2,9 \cdot 10^{-7}$
k_{eff}			$3,3 \cdot 10^{-6}$

Table 4.24: Results of uncertainty budget Biolever

4.4.6 ParkSystems PPP NCHR uncertainty budget

Parameter	$u^2(x_i)$	$\left(\frac{\partial k_S}{\partial x_i}\right)$	$u_c^2(y)$
b	$6,9 \cdot 10^{-13}$	$1,6 \cdot 10^{+6}$	$1,8$
L	$1,1 \cdot 10^{-13}$	$2,3 \cdot 10^{+5}$	$5,6 \cdot 10^{-3}$
ρ_{air}	$3,1 \cdot 10^{-7}$	$2,7 \cdot 10^{+1}$	$2,2 \cdot 10^{-4}$
f_R	$1,0 \cdot 10^{+2}$	$2,1 \cdot 10^{-4}$	$4,2 \cdot 10^{-6}$
Q	$5,5 \cdot 10^{+1}$	$7,0 \cdot 10^{-2}$	$2,7 \cdot 10^{-1}$
$\Gamma_{i,rect}(\omega)$	$4,49 \cdot 10^{-4}$	$6,4 \cdot 10^{+1}$	$1,8$
k			$3,9$
k	$3,9$	$1,3$	$6,8$
L	$1,1 \cdot 10^{-13}$	$-9,0 \cdot 10^{4}$	$8,9 \cdot 10^{-4}$
ΔL	$8,4 \cdot 10^{-14}$	$1,0 \cdot 10^{6}$	$8,4 \cdot 10^{-2}$
k_{eff}			6,9

Table 4.25: Results of uncertainty budget Park

4.4.7 Considerations on the results in propagation of uncertainties

Analyzing the results, it becomes clear that the parameters that most influence the value of the elastic constant k are the dimensional parameters b and L, with b having a greater impact as it appears squared in Sader's formula. The quality factor Q also significantly affects the result, as it strongly depends on the chosen windowing and is difficult to determine with high precision.

Regarding the uncertainty of k_{eff}, it can be observed that, since the uncertainty of k is propagated, it is equal to or of the same order of magnitude as k, therefore the uncertainties associated with ΔL and L contribute to the overall uncertainty, but their impact remains relatively small.

4.5 Elastic constant in dynamic conditions results

The final values for the parameters k and k_{eff}, derived from the analyses conducted in this study, are presented in Table 4.26. In addition, Table 4.27 is contains a detailed summary of the uncertainties associated with k_{eff}, including both the combined standard uncertainty and the expanded uncertainty, calculated in accordance with the methodologies described in Section 3.1.2.

Cantilever	k_{eff}	k	Unit
Atec ContAu	-	0,13	N/m
MikroMasch CSC38			N/m
Cantilever A	0,21	0,17	N/m
Cantilever B	0,05	0,04	N/m
Cantilever C	0,09	0,08	N/m
Bruker NPG10			N/m
Cantilever A	0,50	0,45	N/m
Cantilever B	0,15	0,14	N/m
Cantilever C	0,23	0,21	N/m
Cantilever D	0,022	0,021	N/m
MikroMasch XSC11			N/m
Cantilever A	0,21	0,20	N/m
Cantilever B	4,57	3,98	N/m
Olympus Biolever	0,11	0,08	N/m
ParkSystems PPP NCHR	40,47	30,44	N/m

Table 4.26: Comparison of effective and normal spring constant results

The spring constants, both normal and effective, for cantilevers used in biomedical applications are found to be less than 1 N/m, with the exception of the Park cantilever, used in mechanical applications, which has a significantly higher spring constant, reflecting its greater stiffness.

Cantilever	$u(k_{eff})$	$U(k_{eff})$
Atec ContAu	-	-
MikroMasch CSC38		
Cantilever A	$1,4 \cdot 10^{-2}$	0,028
Cantilever B	$3,1 \cdot 10^{-3}$	0,006
Cantilever C	$6,6 \cdot 10^{-3}$	0,014
Bruker NPG10		
Cantilever A	$8,5 \cdot 10^{-3}$	0,017
Cantilever B	$7,7 \cdot 10^{-3}$	0,016
Cantilever C	$1,5 \cdot 10^{-2}$	0,031
Cantilever D	$8,7 \cdot 10^{-4}$	0,002
MikroMasch XSC11		
Cantilever A	$2,3 \cdot 10^{-2}$	0,047
Cantilever B	$3,4 \cdot 10^{-1}$	0,691
Olympus Biolever	$1,8 \cdot 10^{-3}$	0,004
ParkSystems PPP NCHR	$2,6$	5,4

Table 4.27: Standard and expantended uncertainty of effective spring constant

Another relevant observation concerns uncertainties: it is observed that, as the stiffness of the cantilever increases, the standard and extended uncertainty tend to increase. This behavior is further highlighted in Section 4.4, relating to the propagation of uncertainties. The greater stiffness of cantilevers implies a greater sensitivity with respect to dimensional uncertainties, which significantly influence the final uncertainty. The deflections in the stiffer cantilevers are in fact reduced, but small inaccuracies in the length and thickness measurements are more influential, amplifying the overall uncertainty.

4.6 Elastic constant in static conditions results

The elastic constant calculated up to now refers to the dynamic modulus, i.e. considering the cantilever's response to loads that vary over time, as in the case of oscillations caused by air. The cantilever is therefore subjected to vibrations and therefore produces a dynamic response. In static conditions, however, the cantilever is subjected to constant loads (stress) over time and produces a proportional deformation (strain) from which the static elastic constant of the cantilever is obtained. This cannot automatically be assumed to be equal to the dynamic one since we are not in a condition of pure shear stress, which if isothermal is also reversible and therefore isentropic. In compression and traction, if a process is isothermal, it cannot also be assumed to be isentropic and consequently the two elastic moduli, static (isentropic) and dynamic (isothermal), differ [31]:

$$k_{st} = \frac{k_{dyn}}{1 + \frac{T\alpha^2}{9\ \rho\ c_P} k_{dyn} \frac{L}{bh}} \tag{4.1}$$

where:

- T is the temperature at which the cantilever is analyzed in Kelvin;
- ρ is the density of the cantilever's material, c_P its specific heat capacity at constant pressure and α is the coefficient of thermal expansivity;
- $L,\ b,\ h$ are the dimensional parameters of the cantilever.

Silicon Nitride (Si_3N_4) was considered as a reference material for mechanical properties, since all analyzed cantilevers have a core made of silicon or silicon nitride. The latter, however, does not show significant differences compared to silicon in terms of mechanical and thermal property values.

Parameter	Value	Unit
Specific heat (c_p)	0.673	J/(g·K)
Thermal expansion coefficient (α)	3.3	$10^{-6}\,K^{-1}$
Density (ρ)	2330	kg/m^3

Table 4.28: Material properties of silicon nitride

It has also been shown by Sader in [9], that the coating of the cantilever, which is often gold, does not affect the result of the elastic constant in any way, so it will not be accounted for.

Cantilever	k_{st}/k_{dyn}
Atec ContAu	1,000
MikroMasch CSC38	
Cantilever A	1,000
Cantilever B	1,000
Cantilever C	1,000
Bruker NPG10	
Cantilever A	1,000
Cantilever B	1,000
Cantilever C	1,000
Cantilever D	1,000
MikroMasch XSC11	
Cantilever A	1,000
Cantilever B	1,000
Olympus Biolever	1,000
ParkSystems PPP NCHR	1,000

Table 4.29: Ratio between static and dynamic spring constant results

The results obtained and shown in Table 4.29 indicate that the calculated values for the static elastic modulus and the dynamic elastic modulus are substantially congruent, even considering a high number of decimal places. In the table, however, for reasons of practicality, only the first decimal places are reported. This congruence is found indiscriminately both in cantilevers characterized by a lower stiffness and in those with a higher stiffness. The results also do not change significantly even when considering another material, different compositions or insertions of alloying elements in the materials. It is important to note, however, that the calculation performed is more approximate than others used in this study since the nominal values relating to the material were used and therefore the propagation of uncertainties was not carried out.

4.7 Study of the dynamic response in different analysis points along the cantilever

As mentioned in Section 4.1, the cantilever analysis was conducted at the point furthest from the cantilever base, so the laser was positioned at the tip of the cantilever. An analysis was then conducted to evaluate the variations in the dynamic response of the cantilever as a function of the analysis point along its length.

In particular, the Atec ContAu cantilever and the MikroMasch CSC38 tip B cantilever were selected, as they have the longest length among the available cantilevers. This feature makes them particularly suitable for highlighting the differences between the different investigation points, ensuring greater sensitivity in the study of the dynamic variations along the cantilever axis. Resonance frequency and quality factor values were obtained by applying a Lorentzian fitting to the raw data.

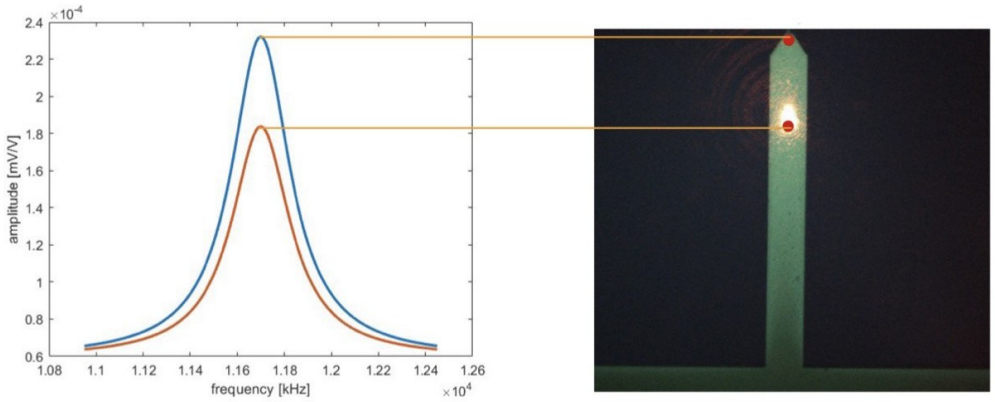

Figure 4.15: Comparison of Atec ContAu dynamic response in different points

Parameter	Tip	Center
Resonant frequency f_R	11700 Hz	11700 Hz
Quality factor Q	48,8	45

Table 4.30: Comparison of Atec ContAu results in different points

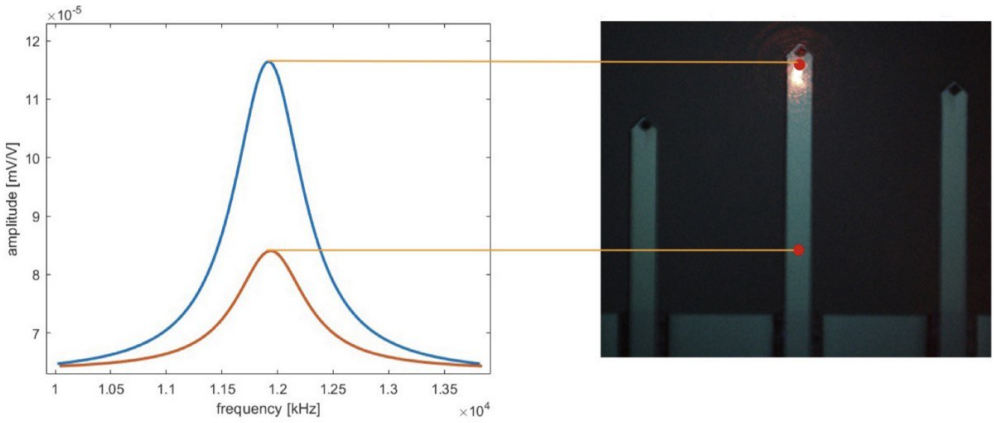

Figure 4.16: Comparison of CSC38 tip B dynamic response in different points

Parameter	Tip	Center
Resonant frequency f_R	11920 Hz	11940 Hz
Quality factor Q	23,00	6,00

Table 4.31: Comparison of MikroMasch CSC38 tip B parameters

As highlighted by the results reported in the tables, the resonance frequency does not show significant variations between the values measured at the tip and the center of the cantilever. On the contrary, the quality factor shows a marked dependence on the analysis point, with the difference becoming more pronounced as the measurement moves further from the tip along the length of the cantilever. In the case of the Atec ContAu cantilever, the measurements were taken at points relatively close to the tip, and the quality factor does not vary significantly, as can be seen from Table 4.30. In contrast, in the case of the MikroMasch CSC38 cantilever, measurements were taken at two points much farther apart along the length of the cantilever, and the quality factor changes dramatically (Table 4.31). The peak amplitude increases proportionally as the measurement is taken near the tip of the cantilever, as expected for a beam with free and locked end conditions.

4.8 Torsional characterization of an AFM cantilever

To accurately determine the value of the friction forces between the cantilever tip and the surfaces, it is necessary to calculate the lateral forces. The latter are obtained from the torsional spring constant of the cantilever, which represents a fundamental parameter for a correct evaluation of the lateral mechanical interactions.

In Figure 4.17, are shown the flexural deflection Δz of a cantilever due to applied normal force N (a) and (b) the torsional deflection $\Delta\phi$ of a cantilever due to applied torque T.

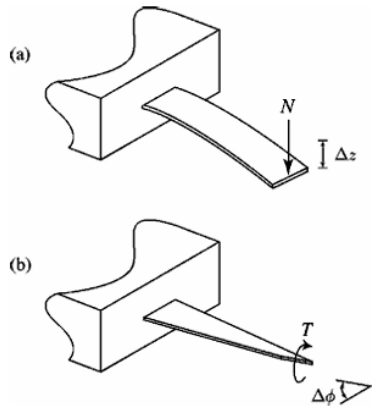

Figure 4.17: Flexural deflection (a) and the torsional deflection (b) [10]

The torsional elastic constant of the cantilever is very difficult to calculate accurately, and many researchers get around this difficulty by making measurements of relative friction by scanning different surfaces with the same cantilever. However, this approach requires that all measurements be made at the same time and very accurately without changing the laser alignment.

To bypass this problem, it would be better to determine the torsional elastic constants of the cantilevers individually [32]. To determine the torsional spring constant we use the formula provided by Sader which is a derivation of the original Sader formula mentioned in Section 3.1.1:

$$k_\phi = 0,1592\rho_{air}\ b^4\ L\ Q_t\ \omega_t^2\ \Gamma_i^t(\omega_t) \tag{4.2}$$

where k_ϕ, expressed in N·m, is the torsional spring constant of the cantilever,

ω_t is the torsional frequency, $\Gamma_i^t(\omega_t)$ is the imaginary part of the hydrodynamic function calculated based on the torsional frequency, Q_t is the quality factor calculated for the torsional case and the other parameters are outlined in Section 3.1.1.

While the already existing parameters in the original Sader's formula 3.10 can be reutilized in this new formula, additional calculations for Q_t, ω_t and $\Gamma_i^t(\omega_t)$ need to be performed.

The adopted equations (4.3), (4.4), (4.5) are used for a preliminary estimate of the torsional resonance frequency of the cantilever. However, the result is approximate for two main reasons.

First, there is no precise measurement of the thickness h of the cantilever, which is a fundamental parameter for the calculations. Second, in the final formula there is a term dependent on the hydrodynamic response function, which is expressed as a function of the torsional frequency itself, which is the object of our analysis.

Therefore, the value calculated through these approximate equations does not represent the final result but serves to identify a plausible interval in which the torsional resonance peak is located. This interval is subsequently examined in the experimental spectrum, allowing to precisely identify the actual torsional resonance frequency.

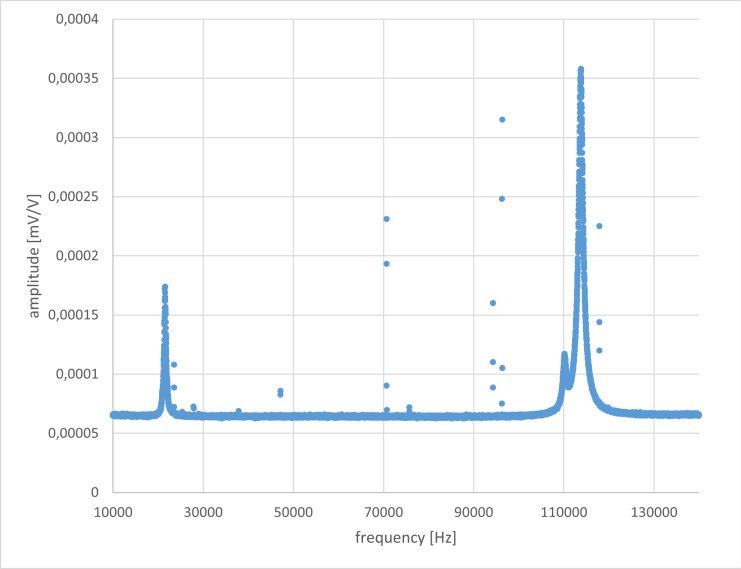

Figure 4.18: Spectrum of Bruker NPG10 tip B showing flexural and torsional resonant frequencies

To obtain the torsional resonance frequency ω_t needed to apply the formula, we must start from the flexural frequency in vacuum ω^f_{vac} which is function of the flexural frequency ω_f with the following equation:

$$\omega^f_{vac} = \omega_f \left(1 + \frac{\pi \rho_{air} b}{4 \rho_c h} \Gamma_r(\omega_f)\right)^{1/2} \tag{4.3}$$

where ρ_{air} is the air density, b is the width of the cantilever, h is the thickness of the cantilever, $\Gamma_r(\omega_f)$ is the real part of the hydrodynamic function, ρ_c is the density of the cantilever and therefore depends on its material.
Subsequently, a correlation is established between the flexural resonance frequency in vacuum and the corresponding torsional frequency, also determined in vacuum conditions as a function of the dimensional parameters and the Poisson's coefficient ν.

$$\frac{\omega^t_{vac}}{\omega^f_{vac}} = 2,1886 \ \frac{L}{b} \sqrt{\frac{1}{1+\nu}} \tag{4.4}$$

And through Formula (4.5), ω_t is retrieved from its value in vacuum conditions.

$$\omega^t_{vac} = \omega_t \left(1 + \frac{3\pi \rho b}{2 \rho_c h} \Gamma^t_r(\omega_t)\right)^{1/2} \tag{4.5}$$

Once the approximate value of the torsional resonance frequency has been identified and the corresponding effective value has been determined through spectrum analysis, the same method described in Section 3.5 is applied. This approach allows obtaining all the parameters necessary for the formulation and accurate calculation of the torsional spring constant of the cantilever. Among the results obtained for the twelve cantilevers analyzed, it was observed that the cantilevers with the highest torsional resonance did not show it in the spectrum. This phenomenon could be attributed to the selected bandwidth or to the background noise detected at high frequencies, as discussed in Section 4.1. These factors could have significantly distorted or hidden the resonance peak.

For this reason, the results related to the torsional spring constant of three representative cantilevers will be reported and analyzed in the following.

Cantilever	k_ϕ [Nm]	$u(k_\phi)$
MikroMasch CSC38		
Cantilever A	$2.018 \cdot 10^{-8}$	$2.3 \cdot 10^{-9}$
Cantilever C	$1.962 \cdot 10^{-8}$	$2.2 \cdot 10^{-9}$
Bruker NPG10		
Cantilever B	$1.072 \cdot 10^{-8}$	$5.5 \cdot 10^{-10}$

Table 4.32: Torsional spring constant and standard uncertainty results for selected cantilevers

The values of the torsional spring constant obtained are particularly low, as anticipated by Sader's papers.

As for the standard uncertainties, the propagation was carried out in the same way as in Section 4.4 for the flexural case. Also in this case the main factors contributing to the uncertainty are related to the dimensional measures and to the quality factor. It should be emphasized that this study, related to the calculation of the torsional spring constant and especially to its metrological characterization, is still in its preliminary stages. In fact, the proposed method is based on several initial approximations that need further verification and optimization. Therefore, the results obtained should be considered as a starting point for future more in-depth investigations and for the improvement of the precision and reliability of the measurement techniques.

Chapter 5

Conclusions

5.1 Conclusions and future developments

The metrological characterization of cantilevers by Atomic Force Microscopy is a crucial aspect of ensuring the accuracy and traceability of measurements, which are essential for determining the rheological and mechanical properties of reference samples, particularly in the biological field. Among many existing methods for metrological calibration of cantilevers, Sader's method was chosen because it provides greater accuracy than others and facilitates the identification of the parameters that most contribute to uncertainty.

The use of the Micro Laser Doppler Vibrometer and the Scanning Electron Microscope available at INRiM allowed to obtain reportable and repeatable values of the resonance frequency and dimensional parameters of the cantilever. In addition, through the use of Lorentzian fitting, it was possible to determine the value of the quality factor with very low uncertainties, thus contributing to a more accurate and reliable calibration.

Twelve tips from six different manufacturers were analyzed, with variations in size and shape. Of these, eleven were soft cantilevers, intended for biological applications, with elastic constants of less than 1 N/m, while one intended for mechanical applications, characterized by a significantly higher elastic constant.

The results obtained for the elastic constant and effective elastic constant were compared with the nominal values, showing good agreement, with an uncertainty of less than 10 percent. In addition, a comparison was made between the dynamic and static elastic constant, showing that the values obtained co-

incide up to a significant number of decimal places.

A comparison of the values of the cantilever elastic constant was also made by shifting the positioning of the measuring point, concluding that this variation affects the result of the quality factor, but not the resonant frequency, which proved to be the parameter with the highest accuracy in determination.

The parameters that contribute most to uncertainty are dimensional parameters, particularly the width, and quality factor. However, the accuracy in measuring the quality factor was greatly improved through the use of Lorentzian fitting. Finally, torsional metrological characterization was introduced, which provided results in line with nominal results.

The importance of torsional metrological characterization lies in the fact that in order to accurately determine the friction forces between the cantilever tip and surfaces, it is necessary to calculate the lateral forces derived from the torsional elastic constant of the cantilever. However, obtaining this value with accuracy and repeatability remains a challenge, since many involved parameters do not yet possess metrological reportability.

Although accurate values have been provided in this thesis, they are still not fully metrologically referable, as they are based on a number of approximations.

Therefore, it will be critical to focus on metrologically determining each term in the formula in order to obtain a complete metrological characterization of the cantilevers, both flexural and torsional.

Bibliography

[1] J.E. Sader, J.W.M. Chon, and P. Mulvaney. Calibration of rectangular atomic force microscope cantilevers. *Review of Scientific Instruments*, 70(10):3967–3969, 1999.

[2] J.E. Sader and L.G. Larsson. Frequency response of cantilever beams immersed in viscous fluids with applications to the atomic force microscope. *Journal of Applied Physics*, 84(1):64–76, 1998.

[3] H.J. Butt and M. Jaschke. Electrostatic interaction in atomic force microscopy. *Physical Review Letters*, 75(15):3106–3109, 1995.

[4] G. Binnig, C.F. Quate, and C. Gerber. Atomic force microscope. *Physical Review Letters*, 56(9):930–933, 1986.

[5] Yitong Qin, Wenguang Yang, Honghui Chu, Yan Li, Shuxiang Cai, Haibo Yu, and Lianqing Liu. Atomic force microscopy for tumor research at cell and molecule levels. *Cambridge University Press*, March 2022.

[6] R. Garcia and R. Perez. Dynamic atomic force microscopy methods. *Surface Science Reports*, 47(6-8):197–301, 2002.

[7] NT-MDT Spectrum Instruments. Cantilever-sample interaction potential. afm operation modes, 2021.

[8] Park Systems. *AFM Probe Selection Guide: How to Choose an AFM Probe*. Park Systems, 2008. Guide document.

[9] J.E. Sader, I. Larson, P. Mulvaney, and L.R. White. Method for the calibration of atomic force microscope cantilevers. *Review of Scientific Instruments*, 66(7):3789–3798, 1995.

[10] Christopher P. Green, Hadi Lioe, Jason P. Cleveland, Roger Proksch, Paul Mulvaney, and John E. Sader. Normal and torsional spring constants of atomic force microscope cantilevers. *Review of Scientific Instruments*, 75(6):1988–1996, 2004.

[11] Vytautas Bučinskas, Darius Viržonis, and Inga Morkvėnaitė-Vilkončienė. Characteristics and functionality of cantilevers and scanners in atomic force microscopy. *Materials*, 16(19):6379, 2023.

[12] SPM Tips. Library of probes and cantilevers. https://www.spmtips.com/library-probes-and-cantilevers, 2024. Accessed: 2024-12-05.

[13] Nano and More. Afm probe cp-contpm. https://www.nanoandmore.com/AFM-Probe-CP-CONT-PM, 2024. Accessed: 2024-12-05.

[14] Guangzhao Guan, Yan He, and Li Mei. Atomic force microscopy: A nanobiotechnology for cellular research. *NTM & Technology*, 2022(9130004), 2022.

[15] J. Smith and A. Johnson. Mechanical measurements of cells using afm: 3d or 2d physics? *Frontiers in Bioengineering and Biotechnology*, 8, November 2020.

[16] Hermann Schillers, Carmela Rianna, and Schäpe. Standardized nanomechanical atomic force microscopy procedure (snap) for measuring soft and biological samples. *Nature Protocols*, 12(2):1–27, 2017.

[17] A. Levillain, C.B. Confavreux, M. Decaussin-Petrucci, E. Durieux, P. Paparel, K. Le-Bail Carval, L. Maillard, F. Bermond, D. Mitton, and H. Follet. Mechanical properties of breast, kidney, and thyroid tumours measured by afm: Relationship with tissue structure. *Materials Today Advances*, 13:101555, 2022.

[18] M. Lekka, P. Laidler, D. Gil, J. Lekki, Z. Stachura, and A. Z. Hrynkiewicz.

Elasticity of normal and cancerous human bladder cells studied by scanning force microscopy. *European Biophysics Journal*, 28(4):312–316, 2001.

[19] D.J. Thompson and R. Smith. Direct measurement of cantilever spring constants using static methods. *Applied Physics Letters*, 80(3):460–462, 2002.

[20] J. P. Cleveland, S. Manne, D. Bocek, and P. K. Hansma. A nondestructive method for determining the spring constant of cantilevers for scanning force microscopy. *Review of Scientific Instruments*, 64(2):403–405, 1993.

[21] Ashley D. Slattery, Jamie S. Quinton, and Christopher T. Gibson. Atomic force microscope cantilever calibration using a focused ion beam. *Nanotechnology*, 23(28):285704, 2012.

[22] J. L. Hutter and J. Bechhoefer. Calibration of atomic force microscope tips. *Review of Scientific Instruments*, 64(7):1868–1873, 1993.

[23] Joost te Riet, Allard J. Katanc, and Christian Rankl. Interlaboratory round robin on cantilever calibration for afm force spectroscopy. *Review of Scientific Instruments*, 82(11):113704, 2011. Received 13 July 2011; received in revised form 12 September 2011; accepted 16 September 2011; available online 24 September 2011.

[24] S. Timoshenko and S. Woinowsky-Krieger. *Theory of Plates and Shells*. McGraw-Hill, New York, 1959.

[25] A.W. Leissa. The historical bases of the rayleigh and ritz methods. *Journal of Sound and Vibration*, 75(2):253–263, 1981.

[26] K. Rasmussen. Calculation methods for the physical properties of air used in the calibration of microphones. Report PL-11b, Technical University of Denmark, Lyngby, Denmark, 1997.

[27] John Elie Sader. Frequency response of cantilever beams immersed in viscous fluids with applications to the atomic force microscope. *Journal of Applied Physics*, 84(1):64–76, July 1998.

[28] Joint Committee for Guides in Metrology (JCGM). *Evaluation of Measurement Data — Guide to the Expression of Uncertainty in Measurement*. Bureau International des Poids et Mesures (BIPM), Sèvres, France, 1st, with minor corrections edition, 2008.

[29] A. Fasana and N. Marchisello. *Meccanica delle vibrazioni*. McGraw-Hill Education, Milano, Italia, 2015.

[30] G.W.F. Drake. *Atomic, Molecular, and Optical Physics Handbook*. AIP Press, Woodbury, NY, 1996.

[31] Anthony Goodwin, K. N. Marsh, and W. A. Wakeham. *Measurement of the Thermodynamic Properties of Single Phases*. Elsevier, Amsterdam, Netherlands, 2003.

[32] Richard S. Gates and Jon R. Pratt. Accurate and precise calibration of afm cantilever spring constants using laser doppler vibrometry. *Nanotechnology*, 23:375702, 2012.